

We are IntechOpen, the world's leading publisher of Open Access books Built by scientists, for scientists

6,900

Open access books available

186,000

International authors and editors

200M

Downloads

Our authors are among the

154

Countries delivered to

TOP 1%

most cited scientists

12.2%

Contributors from top 500 universities



WEB OF SCIENCE™

Selection of our books indexed in the Book Citation Index
in Web of Science™ Core Collection (BKCI)

Interested in publishing with us?
Contact book.department@intechopen.com

Numbers displayed above are based on latest data collected.
For more information visit www.intechopen.com



Nano/Micro-Patterning of Metal Oxide Nanocrystals

Yoshitake Masuda

*National Institute of Advanced Industrial Science and Technology (AIST)
Anagahora, Shimoshidami, Moriyama-ku, Nagoya
Japan*

1. Introduction

Metal oxides have recently been fabricated in solutions without high-temperature sintering in order to reduce energy consumption and allow application for various substrates having low heat resistance. The fabrication of metal oxide thin films from solutions has been encouraged by the development of environment-friendly chemistry such as Green & sustainable chemistry¹⁻⁶, Bioinspired materials chemistry⁷, Biomimetic materials chemistry⁷, Soft-solution processing⁸⁻¹⁰, Soft chemistry (“Chimie douce” in French)¹¹, Liquid phase deposition^{7,12}, Chemical bath deposition (CBD)^{12,13}, Electroless deposition (ED) with catalyst^{12,13}, Successive ion layer adsorption and reaction (SILAR)^{12,13}, Sol-gel process^{14,15}, Hydrothermal reaction¹⁶, Electrodeposition^{17,18} and so on. Solution processing of metal oxides allows us to prepare metal oxide thin films on the surface of solids such as substrates, particles, and fibers. Metal oxide nano/microstructures can also be fabricated by applying these solution systems to electronic or photonic devices.

Many kinds of lithography or patterning techniques have been developed to prepare patterns of thin films, for instance, X-ray/electronbeam lithography and photolithography,¹⁹ microcontact printing,^{20,21} wet etching,²² ink-jet printing,²³ embossing,^{24,25} slip-pressing,²⁶ charge-based printing,²⁷ micromolding,²⁸ and cold welding²⁹. However, etching or lift-off processes are required in many of these methods, which causes degradation of performance, increases waste and energy consumption, and makes the process complicated. Additionally, etching or lift-off processes cannot be applied to corrosion-resistant metal oxides. The deposition of metal oxides only on desired areas of a substrate is thus required for the patterning of metal oxide thin films.

In this section, Liquid Phase Patterning (LPP) of metal oxides was reported³⁰. Self-assembled monolayer (SAM), which can modify the surface of solids with various functional groups, was used as the template to enable molecular recognition for LPP. Solution systems were developed and applied to LPP of ceramic thin films on patterned SAMs by the proposed novel LPP processes.

2. Liquid phase patterning of metal oxides

2.1 SAM preparation for patterning of metal oxides

Self-assembled monolayer (SAM) can modify the surface of solids such as a substrate, particles, or fibers with various functional groups, and the molecular recognition of

functional groups of SAM was the key technique for LPP. Patterned SAMs were used as templates in our LPP processes to deposit metal oxide thin films on desired areas of substrates.

An Si wafer (p-type Si [100], NK Platz Co., Ltd.) was sonicated in water, ethanol or acetone for 10 min, respectively, and exposed for 15 min to UV light (184.9 nm and 253.7 nm) (low-pressure mercury lamp 200 W, PL21-200, 15 mW/cm² for 254 nm, SEN Lights Co.) to clean the surface. UV light (PL21-200) has stronger power than that used in former studies (NL-UV253, Nippon Laser & Electronics Lab.). The OTS(octadecyltrichlorosilane, C₁₈H₃₇SiCl₃)-SAM or APTS(aminopropyltrimethoxysilane, H₂NC₃H₅Si(OCH₃)₃) were prepared by immersing the Si substrate in an anhydrous toluene (Aldrich Chemical Co., Inc.) solution containing 1 vol% OTS (Acros Organics) for 15 min or APTS (TCI) for 2 h under an N₂ atmosphere ^{31,32}(Fig. 1). The substrate with the SAM was baked at 120°C for 5 min to remove residual solvent and promote chemisorption of the SAM. The control of preparation conditions such as humidity is very important to fabricate organically modified surfaces which realize site-selective deposition.

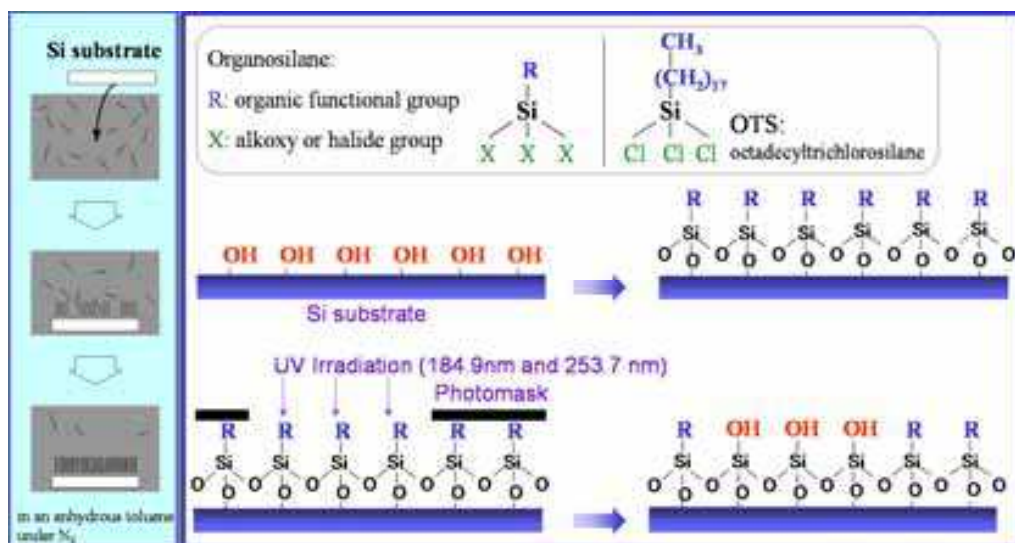


Fig. 1. Conceptual process for fabrication of a self-assembled monolayer.

Reprinted with permission from Ref.³¹, Masuda, Y., Gao, Y. F., Zhu, P. X., Shirahata, N., Saito, N. and Koumoto, K., 2004, *J. Ceram. Soc. Japan*, 112, 1495. Copyright © The Ceramic Society of Japan

The SAMs on the silicon substrates were exposed for 15 min to UV light through a photomask to be used as a template for micropatterning of ZnO crystals. UV-irradiated regions became hydrophilic due to silanol group formation, while the non-irradiated part remained unchanged. Formation of the SAMs and the modification to silanol groups by UV irradiation were verified using the static water drop contact angle (θ_w) (a contact angle meter CA-D, Kyowa Interface Science Co., Ltd.) and X-ray photoelectron spectroscopy (XPS) (ESCALAB 210, VG Scientific Ltd.). The X-ray source (MgK α , 1253.6 eV) was operated at 15 kV and 18 mA, and the analysis chamber pressure was 1-3 \times 10⁻⁷ Pa. The initially deposited OTS-SAM or APTS-SAM showed a static water contact angle of 105° or 63°, but the UV-irradiated surface of SAM was wetted completely (contact angle < 5°) ³³ (Fig. 2). The spectrum peak corresponding to the N 1s binding energy centered at 399.5 eV was observed for the surface of the APTS-treated Si substrate on which APTS-SAM was formed, however,

it wasn't detected from the surface after UV irradiation. These experiments show the decomposition and removal of SAMs from the surface of substrates.

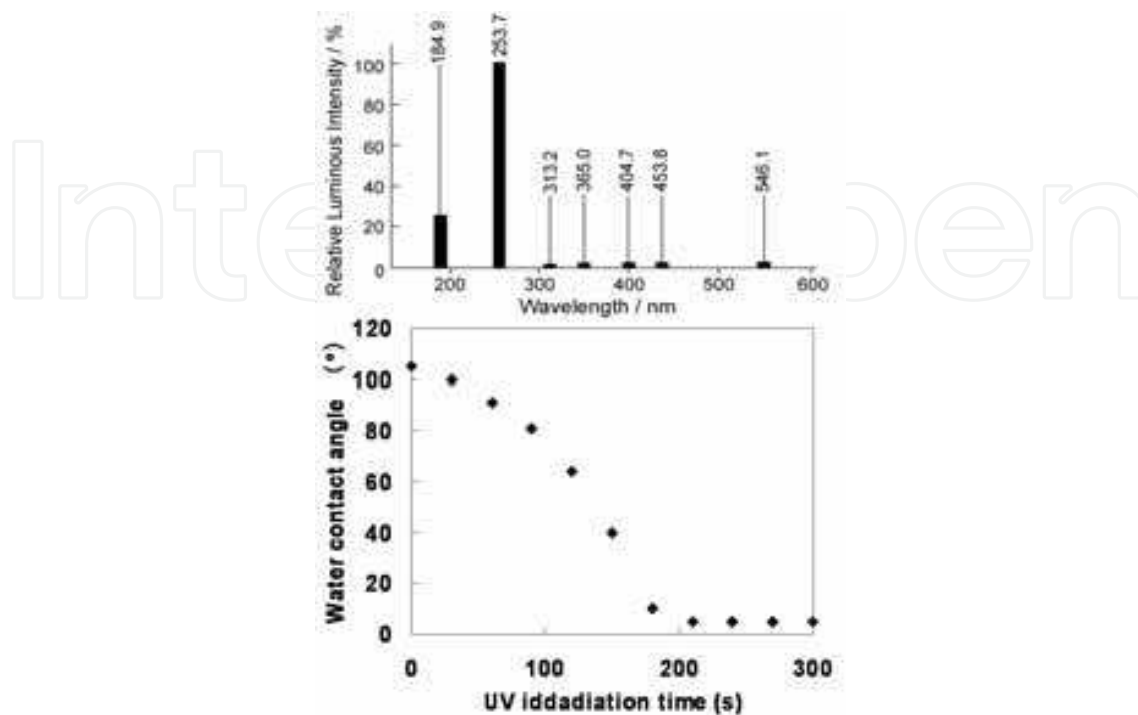


Fig. 2. Relative luminous intensity of UV lamp and water drop contact angle of OTS-SAMs as a function of UV-irradiation time.

Reprinted with permission from Ref. ³³, Masuda, Y., Kinoshita, N., Sato, F. and Koumoto, K., 2006, *Cryst. Growth Des.*, 6, 75. Copyright © American Chemical Society

2.2 Liquid phase patterning of amorphous TiO₂ thin films³⁴⁻³⁷

Patterned OTS-SAM was immersed in an anhydrous toluene (99.8%, water < 0.002%, Aldrich) solution containing 0.1 M TDD (titanium dichloride diethoxide) for 30 min under an N₂ atmosphere using a glove box (Fig. 3)³⁴⁻³⁷. All glassware was dried in a dry box at 50°C before use. The estimated partial pressure of H₂O in an N₂ atmosphere is below 0.1 hPa. Chlorine atoms of TDD react with H₂O and change into OH, which further react with silanol groups of SAM resulting in the formation of Ti-O-Si bonds³⁸. The ethoxy group, OC₂H₅, of TDD is hydrolyzed into hydroxyl groups which are further condensed to form Ti-O-Ti bonds³⁸. The thickness of films can be easily controlled by varying the soaking time. After SAM substrates had been rinsed with toluene and preserved in air, thin films appeared on the silanol surfaces of OTS-SAM but were not observed on octadecyl surfaces³⁴ (Fig. 4). A micropattern of amorphous TiO₂ thin films was thus fabricated on a patterned OTS-SAM. Line width measurements at 15 equally spaced points on each line indicated an average printed line width of 23.3 μm. Line edge roughness, as measured by the standard deviation of the line width, was ~0.5 μm, representing a ~2.1% variation (i.e., 0.5/23.2) in the nominal line width³⁴. X-ray diffraction measurements (XRD) (Rigaku RU-200) with CuKα radiation (40 kV, 30 mA) for as-deposited thin films showed that they were composed of amorphous phases. The ratio of oxygen to titanium was evaluated after 20 min of Ar⁺ ion sputtering to avoid the influence of the contaminated layer on the surface. The 1s peak of O can be deconvoluted into two curves (ratio of 529.7 eV (films) and 531.3 eV (silicon oxide) is 1 :

0.22). The ratio of oxygen to titanium was estimated to be 2.2 : 1. Small amounts of chlorine and carbon were also detected (Ti : O : Cl : C = 1 : 2.2 : 0.17 : 0.37)³⁴.

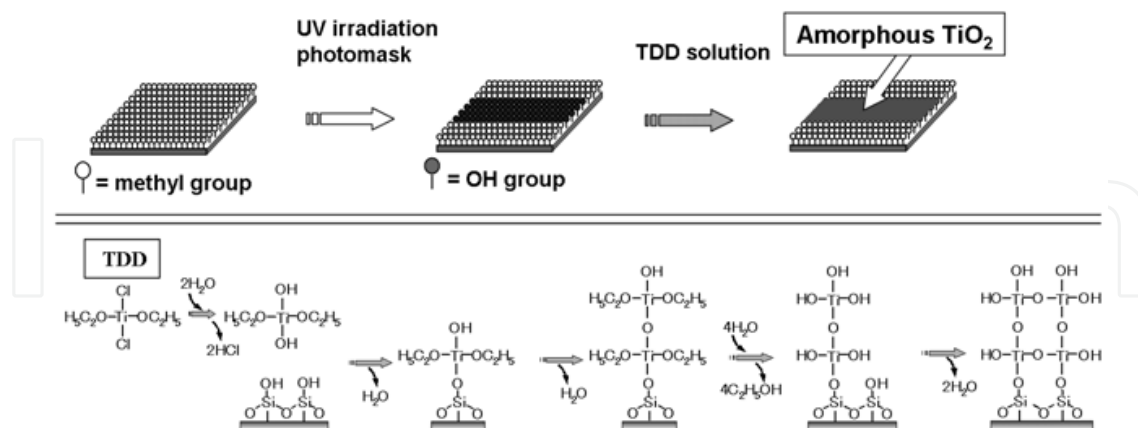


Fig. 3. Conceptual process for selective deposition of amorphous TiO_2 thin film using a self-assembled monolayer.

Reprinted with permission from Ref. ³⁴, Masuda, Y., Sugiyama, T., Lin, H., Seo, W. S. and Koumoto, K., 2001, *Thin Solid Films*, 382, 153. Copyright © Elsevier B.V.

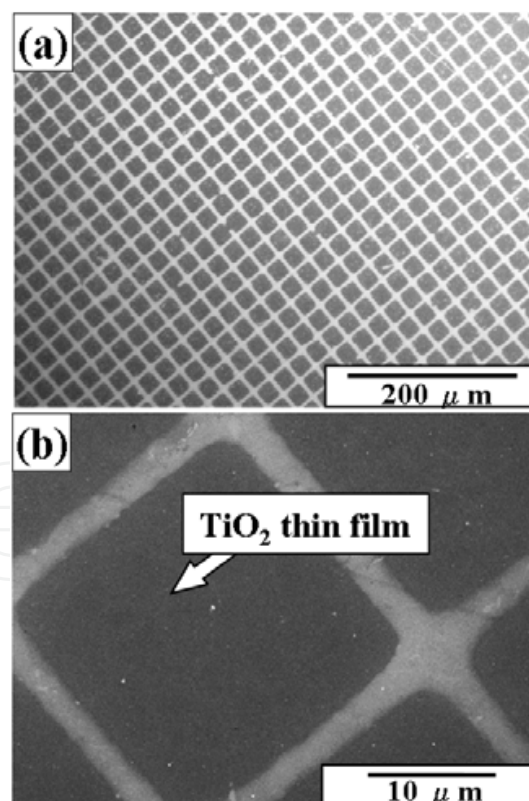


Fig. 4. SEM micrographs of (a) a micropattern of amorphous TiO_2 thin films and (b) magnified area of (a).

Reprinted with permission from Ref. ³⁴, Masuda, Y., Sugiyama, T., Lin, H., Seo, W. S. and Koumoto, K., 2001, *Thin Solid Films*, 382, 153. Copyright © Elsevier B.V.

2.3 Liquid phase patterning of crystalline anatase TiO₂ thin films using a seed layer³⁹

The concept of LPP using a seed layer which accelerates the deposition of thin films was proposed³⁹. The deposition process of anatase TiO₂ from an aqueous solution was evaluated in detail using a quartz crystal microbalance, and it was found that the nucleation and initial growth of anatase TiO₂ were accelerated on amorphous TiO₂ thin films compared with silanol, amino, phenyl, or octadecyl groups. Amorphous TiO₂ thin films were deposited on silanol regions of a patterned OTS-SAM (Fig. 5(1-a,b)) from a TDD solution (Fig. 5(2-a,b)). This substrate was immersed in an aqueous solution containing a Ti precursor at pH 1.5 for 1 h to be used as a template for LPP. Anatase TiO₂ was selectively deposited on amorphous TiO₂ regions to form thin films. Consequently, a micropattern of anatase TiO₂ thin film which had high feature edge acuity was successfully fabricated in an aqueous solution (Fig. 5(3-a,b)). The center of the anatase TiO₂ thin film region was 61 nm higher than the octadecyl regions, and the thickness of the anatase TiO₂ thin film was estimated to be 36 nm

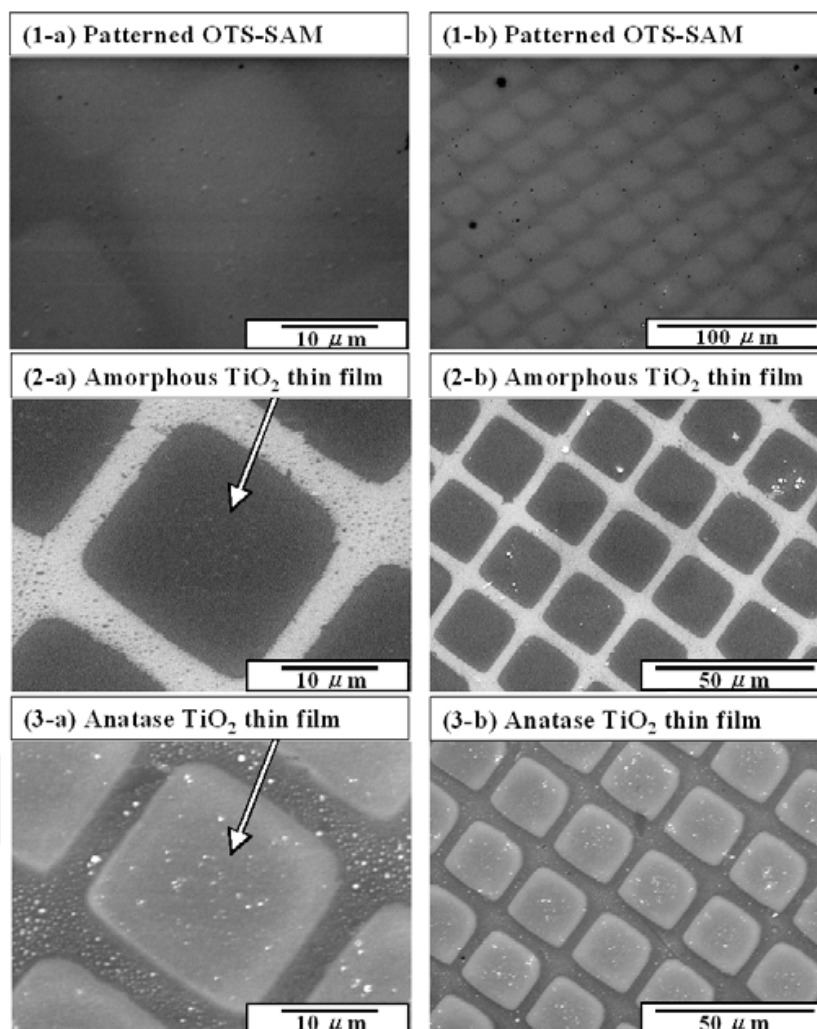


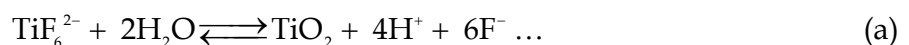
Fig. 5. SEM micrographs of [(1-a), (1-b)] a patterned OTS-SAM, [(2-a), (2-b)] a micropattern of amorphous TiO₂ thin films, and [(3-a), (3-b)] a micropattern of anatase TiO₂ thin films deposited at pH 1.5.

Reprinted with permission from Ref. ³⁹, Masuda, Y., Ieda, S. and Koumoto, K., 2003, *Langmuir*, 19, 4415. Copyright © American Chemical Society

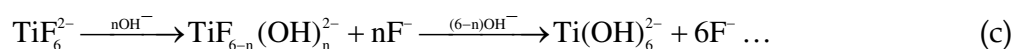
considering the thickness of amorphous TiO₂ thin film (27 nm)³⁴ and OTS molecules (2.4 nm)³⁹. This result is similar to that estimated by QCM measurement (36 nm). The AFM image showed the film roughness to be 3.7 nm (horizontal distance between measurement points: 6.0 μm), which is less than that of amorphous TiO₂ thin film (RMS 9.7 nm, 27 nm thick, horizontal distance between measurement points: 6.0 μm)³⁴. Additionally, the roughness of the octadecyl group regions was shown to be 0.63 nm (horizontal distance between measurement points: 1.8 μm)³⁹. This study showed the good performance of the LPP process using a seed layer and the importance of quantitative analysis of the deposition process.

2.4 Liquid phase patterning of crystalline anatase TiO₂ thin films using site-selective elimination⁴⁰

Ammonium hexafluorotitanate ([NH₄]₂TiF₆) (purity 96%, 1.031 g) and boric acid (H₃BO₃) (purity 99.5%, 0.932 g) were dissolved separately in deionized water (50°C, 50 ml)⁴⁰. An appropriate amount of HCl was added to the boric acid solution to control pH, and ammonium hexafluorotitanate solution was added. Solutions (100 ml) with 0, 0.1 or 0.6 ml of HCl showed pH 3.8, 2.8 or 1.5, respectively. Supersaturation of solution can be changed by pH value as discussed in ref. 55. TiO₂ thin films can be formed fast by the deposition of homogeneously nucleated particles at high pH condition such as pH 3.88, and uniform films can be obtained slowly by heterogeneous nucleation at low pH condition. SAMs were immersed in the solution (100 ml) containing 0.05 M (NH₄)₂TiF₆ and 0.15 M (H₃BO₃) at pH 1.5, 2.8 or 3.8 and kept at 50°C for 4 h. to deposit anatase TiO₂. Ultrasonication was done during immersion period. Deposition of TiO₂ proceeded by the following mechanism:



Equation (a) is described in detail by the following two equations:



Fluorinated titanium complex ions gradually change into titanium hydroxide complex ions in an aqueous solution as shown in Eq. (c). Increase of F⁻ concentration displaces the Eq. (a) and (c) to the left, however, produced F⁻ can be scavenged by H₃BO₃ (BO₃³⁻) as shown in Eq. (b) to displace the Eq. (a) and (c) to the right. Anatase TiO₂ was formed from titanium hydroxide complex ions (Ti(OH)₆²⁻) in Eq. (d), and thus the supersaturation degree and the deposition rate of TiO₂ depend on the concentration of titanium hydroxide complex ions. The high concentration of H⁺ displaces the equilibrium to the left in Eq. (a), and the low concentration of OH⁻, which is replaced with F⁻ ions, suppresses ligand exchange in Eq. (c) and decreases the concentration of titanium hydroxide complex ions at low pH such as pH 1.5. The solution actually remained clear at pH 1.5, showing its low degree of supersaturation. On the other hand, the solution at high pH such as pH 2.8 or 3.8 became turbid because of homogeneously-nucleated anatase TiO₂ particles caused by a high degree of supersaturation. Anatase TiO₂ thin film was formed by heterogeneous nucleation in the

solution at pH 1.5, while the film was formed by heterogeneous nucleation and deposition of homogeneously nucleated particles at pH 2.8 or 3.8.

After having been immersed in the solution with ultrasonic treatment, the substrates were rinsed with distilled water. Thin films were observed on the silanol group regions to form nano/micro-scaled patterns at pH 3.88, 2.8 or 1.5. The films were deposited for 4 h from the solution without the addition of HCl. Thin films were observed as being dark in an optical micrograph. Separated parallel lines 200–400 nm in width at 100–200 nm intervals were successfully fabricated with this method. The length of the separated parallel lines reached more than 100 μm . A cross section of the lines was shown as a semicircle, and the thickness of the center of the lines was estimated to be about 100 nm by AFM observation (Fig. 6). Feature edge acuity of the pattern was higher than that of the pattern fabricated by our lift-off process or by the site-selective immersion method.⁴¹ Site-selective deposition was realized at any pH conditions such as pH 3.88, 2.8 or 1.5. Patterns which have higher feature edge acuity can be obtained at low pH conditions because films were formed slowly without the deposition of homogeneously nucleated particles.

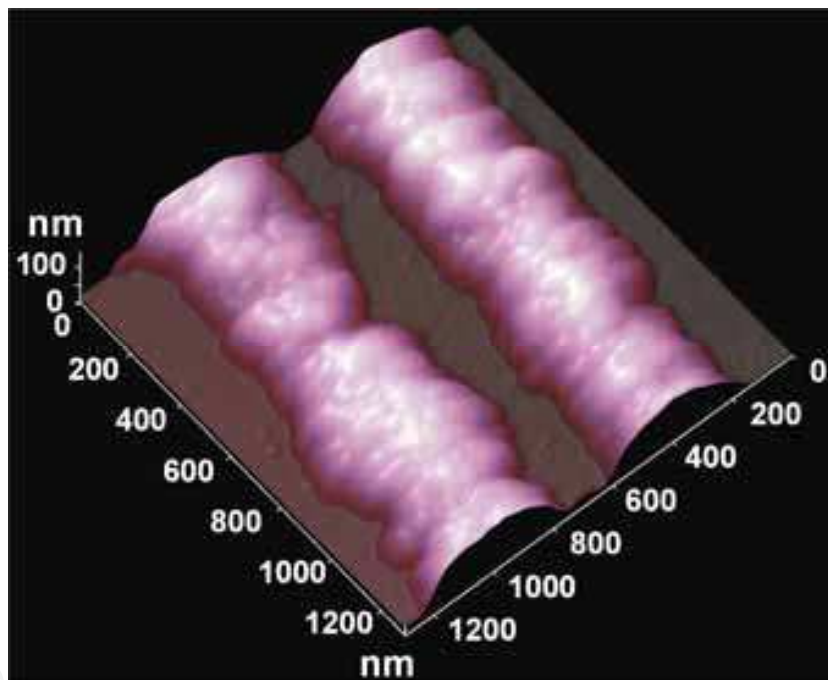


Fig. 6. AFM image of a nanopattern of anatase TiO_2 fabricated by site-selective elimination. Reprinted with permission from Ref. ⁴⁰, Masuda, Y., Saito, N., Hoffmann, R., De Guire, M. R. and Koumoto, K., 2003, *Sci. Tech. Adv. Mater.*, 4, 461. Copyright @ American Chemical Society

For the adhesion of TiO_2 films to silanol groups, the pH of the deposition solution is critical. Pizem *et al.*¹³ reported that adherent TiO_2 films formed from solutions similar to those used here at pH=3.9, but that the films were less adherent at pH=2.9. They related this difference in adherence to an increased electrostatic attraction of TiO_2 to the oxidized surface of silicon at the higher pH. In our experiment, there also were less adherence of TiO_2 at pH 2.8 and 1.5 than that at pH 3.5 due to low supersaturation shown in Eq. (a) and low electrostatic attraction.¹³

However, some depositions were observed on octadecyl group regions in SEM micrographs. One probable cause is that pinholes and other defects in the films provide at least some degree of access of water to underlying unreacted OH groups in the OTS films. Once exposed to the solution, these sites can act as nucleation points for TiO_2 growth. Because the depositions are performed at elevated temperatures, it is likely that pinholes and defects will continually open and close on the OTS film surfaces due to thermal motions of alkyl chains in the films. The TiO_2 precursors formed in these defects would act as points for eventual growth of TiO_2 over the entire SAM-covered region. This would provide a weakly bound TiO_2 film on the OTS film regions due to the limited number of connections to the underlying silanol sites in the film regions. In fact, Sagiv and others have shown that macroscopic defects induced in alkylsiloxane films can readily be accessed by solution species.⁴²⁻⁴⁴ More recently, Dressick and coworkers demonstrated that solvent accessibility to underlying substrates in aromatic siloxane films is also important⁴⁵⁻⁴⁷ and may be an even greater factor in controlling the properties of those films, which may account for our previous selectivity observation using phenylsiloxane films, as shown in the lift-off process. In the lift-off process⁴⁸, thin films were formed on the entire area of patterned SAM that has silanol group regions and phenyl (or octadecyl) group regions. After being dried, the substrate was sonicated in water to lift off thin films on phenyl (or octadecyl) group regions selectively. Thin films on phenyl (or octadecyl) group regions were peeled off along the cracks that formed during the drying process. Thin films on phenyl (or octadecyl) group regions without cracks were not peeled off because depositions strongly connected to each other to form solid timber (monolith). The lift-off along cracks decreased the feature edge acuity of the pattern in this method. Thin films were formed on silanol group regions selectively and site-selective deposition was realized with our newly developed method. This resulted in high feature edge acuity of the patterns compared to our previous works.⁴⁸ Additionally, the micropattern of thin films was also fabricated by the site-selective immersion method⁴¹. A solution containing a Ti precursor contacted the hydrophilic regions during the experiment and briefly came into contact with the hydrophobic regions. The solution on the hydrophilic surface was replaced with a fresh solution by continuous movement of bubbles. Thus TiO_2 was deposited and a thin film was grown on the hydrophilic regions selectively. This technique can be applied for the formation of many kinds of films from any solution and to fabricate micropatterns for many kinds of thin film because the technique creates the difference in contact time of the solution between hydrophilic regions and hydrophobic regions. However, it is difficult to form a solution layer on nano-scaled hydrophilic regions selectively and replace it with a fresh solution by continuous movement of bubbles while avoiding contact of the solution on hydrophobic regions. This prevents fabrication of nano-scaled pattern with this method. On the other hand, site-selective deposition was realized in the solution with our newly developed method using the difference of adhesive strength of depositions to substrates. Heterogeneously nucleated deposition and homogeneously nucleated particles and/or clusters can be removed from octadecyl group regions even if these regions are designed in nano-scale order in which depositions are smaller. This allowed us to realize high feature edge acuity of the patterns compared to site-selective immersion.^{39,41}

The distribution of elements on the surface of the substrates was evaluated by energy dispersive X-ray analysis (EDX; EDAX Falcon, EDAX Co. Ltd.), which is built into SEM. Titanium was detected from thin films selectively and oxygen was detected mainly from silanol group regions by EDX. Other elements, except for silicon from the substrate, were

not observed from the thin film and substrate by EDX. Oxygen was detected from not only the deposited thin film but also from the natural oxide layer (amorphous SiO₂ layer) formed on all surface areas of a silicon substrate. These observations showed predominant deposition of titanium oxide on silanol group regions.

The deposited thin films were also investigated using an X-ray diffractometer (XRD; RAD-C, Rigaku) with CuK α radiation (40 kV, 30 mA) and Ni filter plus a graphite monochromator. Thin films deposited at pH 3.8 for 4 h showed an XRD pattern of anatase-type TiO₂ having orientation similar to that of films deposited in the solution at pH 1.5 or 2.8⁴¹. The diffraction from parallel to c-plane such as (004) was observed as being strong compared to that of the randomly oriented powder diffraction pattern. Pizem *et al.* postulated that the commonly observed [001] orientation of anatase films could be due to the slight polarity of the planes parallel to the [001] axis, unlike other low-index planes of this structure such as {100}, (110), and (210). The orientation and crystal growth mechanism are further discussed in a separate article.⁴⁹

Thin films were further evaluated by X-ray photoelectron spectroscopy (XPS; ESCA-3200, Shimadzu Corporation, 1 \times 10⁻⁵ Pa). The X-ray source (MgK α , 1253.6 eV) was operated at 8 kV and 30 mA. The spectral peaks corresponding to Ti 2p (458.7 eV) were observed from thin films deposited on the silanol region. This binding energy is higher than that of Ti metal (454.0 eV), TiC (454.6 eV), TiO (455.0 eV), TiN (455.7 eV) and Ti₂O₃ (456.7 eV), and similar to that of TiO₂ (458.4 - 458.7 eV).⁵⁰⁻⁵² This suggests that the titanium atoms in thin films are positively charged relative to that of titanium metal by formation of direct bonds with oxygen. On the other hand, this spectrum was not observed from octadecyl group regions. The O 1s spectrum was observed from the silanol regions and divided into O 1s (530.2 eV) and O 1s (532.3 eV). O 1s (532.3 eV) can be assigned to the silicon oxide layer on the surface of the silicon wafer (532.0 eV⁵¹), whereas the binding energy of O 1s (530.2 eV) is similar to that of TiO₂ (529.9 eV⁵², 530.1 eV⁵¹) as observed by Shin *et al.*⁵³. This shows that oxygen is negatively charged compared with neutral oxygen molecules (531.0 eV), possibly through the formation of chemical bonds with Ti. The ratio of titanium to oxygen was estimated from the Ti 2p_{3/2} (458.7 eV) spectrum and O 1s (530.2 eV) spectrum to be Ti:O = 1:2.0.

2.5 Liquid phase patterning of magnetite particulate thin films using Pd catalyst^{54,55}

Catalyst solution containing Na₂PdCl₄ (0.38 mM) and NaCl (0.01 M) in a 0.01 M 2-morpholinoethane sulfonate pH 5 aqueous buffer was prepared^{54,55}. The details of preparation of this solution are described in the reference⁵⁶. Hydrolyzed Pd colloids were formed in this solution.⁵⁷ The patterned APTS-SAM was immersed into the colloidal dispersion of catalyst at 25 °C for 30 min and catalyzed APTS-SAM was rinsed with water.

Catalyzed SAM was immersed in an aqueous solution containing iron(III) nitrate (0.0025 M) and dimethylamine-borane (DMAB) (0.03 M) and kept at 80 °C using a water bath for 30 min to deposit magnetite particulate thin film.⁵⁸ DMAB was used to reduce nitrate ions, giving rise to OH⁻ ions and hence raising the solution pH to precipitate Fe₃O₄.

A black colored iron oxide film selectively deposited onto regions of the APTS-SAM that had not been exposed to UV radiation following application of the Pd catalyst dispersion. Figures 7 show an optical microscope image and a SEM image of as-deposited films, respectively. Black contrast represents a deposited film in an optical microscope image, whereas the white contrast shows deposited films in SEM images. The EDX mapping images shown in Figure 7(c) indicate the films deposited on the amino-surface regions,

showing mapping images consisting mainly of iron and oxygen. Thickness of the films was easily controlled in the range from several ten nano meter to several micro meter by change of immersion period. The XRD pattern of the thin film deposited on the whole surface of the APTS-SAM clearly indicates that it is a magnetite (Fe_3O_4) film composed of randomly oriented crystallites of about 20 nm in diameter, which was evaluated using the Scherer equation. These evaluations show the successful fabrication of a micropattern of crystalline magnetite films in an aqueous solution using a patterned APTS-SAM and Pd colloid catalysts adsorbed on amino-group ($-\text{NH}_2$) regions of a SAM.

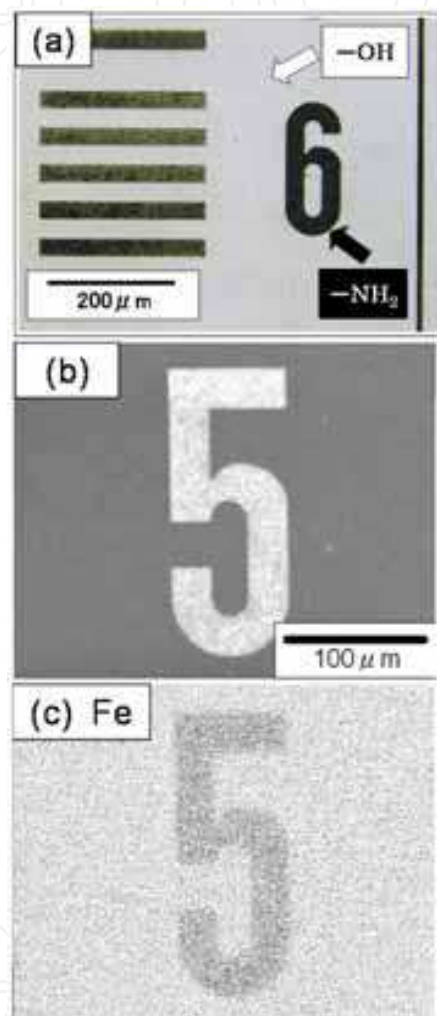


Fig. 7. (a) optical microscope image, (b) SEM image and (c) characteristic X-ray images [Fe] of a micropattern of crystalline Fe_3O_4 .

Reprinted with permission from Ref. ⁵⁴, Nakanishi, T., Masuda, Y. and Koumoto, K., 2004, *Chem. Mater.*, 16, 3484. Copyright © American Chemical Society

2.6 Liquid phase patterning and morphology control of crystalline ZnO ³³

Zinc acetate ($\text{Zn}(\text{CH}_3\text{COO})_2$, Kishida Chemical Co., Ltd.) was dissolved into water to be 15 mM at 50°C , and ammonia (28% solution, Kishida) was then added to be 30, 60 or 90 mM ($[\text{NH}_3] / [\text{Zn}] = 2.0, 4.0$ or 6.0) with stirring as complexing agent³³. These solutions showed pH = 7.04, 7.50 or 8.93, respectively. Zinc ions reacted with ammonium ions (NH_4^+) formed

from ammonia to form tetra amine zinc(II)⁵⁹ $[\text{Zn}(\text{NH}_3)_4]^{2+}$. ZnO was crystallized from the reaction between $[\text{Zn}(\text{NH}_3)_4]^{2+}$ and OH^- . The solution became clouded shortly after adding ammonia due to homogeneous nucleation of ZnO crystals. Morphology of ZnO crystals was controlled by the ratio of ammonia to zinc acetate, i.e., super-saturation degree for crystallization. Patterned OTS-SAMs were immersed downward into the solution containing zinc acetate (15 mM) and ammonia (30 mM) as complexing agent ($[\text{NH}_3] / [\text{Zn}] = 2.0$) at 50°C for 3 h (Fig. 8).

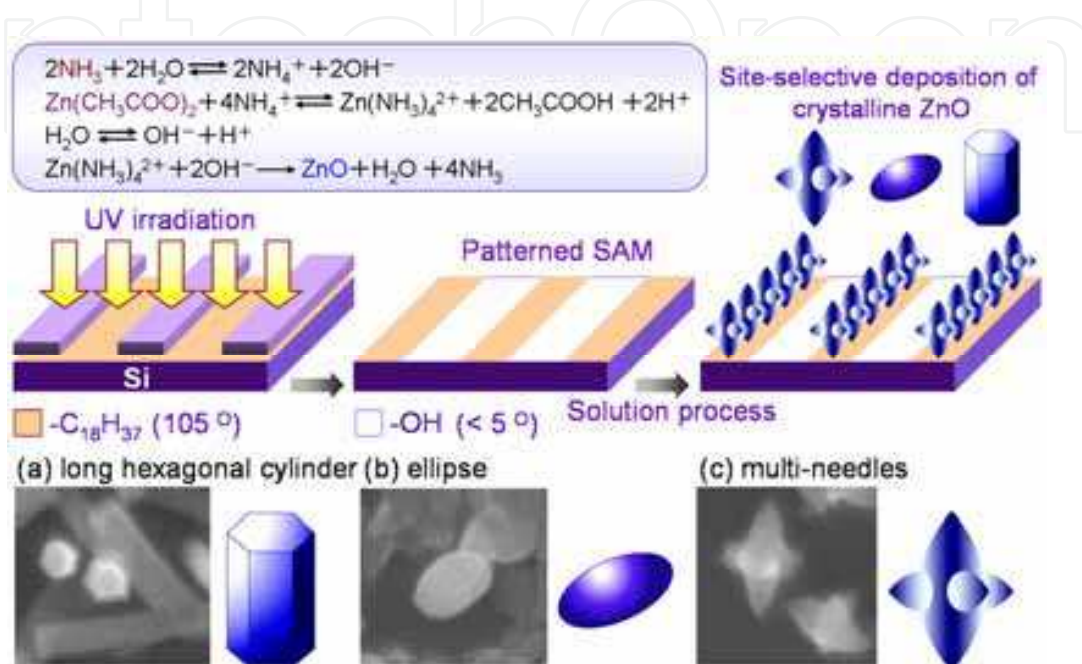


Fig. 8. Conceptual process for self-assembly patterning of light-emitting crystalline ZnO nanoparticles in an aqueous solution.

Reprinted with permission from Ref. ³³, Masuda, Y., Kinoshita, N., Sato, F. and Koumoto, K., 2006, *Cryst. Growth Des.*, 6, 75. Copyright © American Chemical Society

ZnO crystals having long hexagonal cylinder shape were homogeneously nucleated to make the solution turbid shortly after adding ammonia. Crystals showed sharp hexagonal facets of about 100 nm in diameter and larger than 500 nm in length. The morphology indicated high crystallinity of ZnO nanoparticles. The nanoparticles were deposited and further grown on hydrophobic octadecyl group regions of a patterned SAM selectively. Consequently, a micropattern of light-emitting ZnO crystals was successfully fabricated in an aqueous solution without Pd catalyst. ZnO crystals were also deposited on hydrophobic regions of patterned SAMs such as DTS-SAM, HTS-SAM, PIS-SAM, MTS-SAM, PTCS-SAM or APTS-SAM. This showed that the method is highly versatile and offers good potential for the fabrication of devices.

ZnO crystals were deposited on hydrophobic SAM regions such as OTS-, APTS- or other SAMs rather than hydrophilic silanol regions. Zeta potential of ZnO crystals deposited on a silicon substrate was measured to be 10 mV at pH 8.1 and ZnO crystals should thus have positive zeta potential not less than 10 mV in the solution at pH 7.04. SAM of OTS, silanol and APTS showed zeta potential of -3 mV, -38.2 mV or +22.0 mV, respectively. ZnO having positive zeta potential should be deposited on silanol regions having negative zeta potential rather than other SAMs, if the site-selective deposition was caused only by electrostatic

interactions. The site-selective deposition of ZnO crystals would be caused by not only electrostatic interactions as shown by the relation of zeta potentials. ZnO crystals having long hexagonal cylinder shape were deposited on a hydrophilic silicon substrate to evaluate the surface of crystals. The substrate covered with many deposited ZnO crystals exhibited high water contact angle (WCA 140°). The deposited ZnO crystals were found from the experiment to have hydrophobic surfaces. Surfaces of naked ZnO crystals would be hydrophilic because of surface hydroxyl groups and they would become hydrophobic by being covered with organic molecules having hydrophobic functional groups. CH₃COO⁻ ions coming from Zn(CH₃COO)₂ might be adsorbed to ZnO crystal surfaces by the interaction between Zn and -COO⁻ to cover the surface with hydrophobic -CH₃ groups and some of Zn(CH₃COO)₂ would exist in the surface layer of ZnO crystals. Additionally, deposited ZnO crystals having long hexagonal cylinder shape became hydrophilic (< 10°) and their zeta potential shifted positively by UV irradiation in air. ZnO crystals deposited on a silicon substrate showed zeta potential of 10 mV at pH 8.1, 0 mV at pH 8.8 and -15 mV at pH 9.2, while they shifted to 20 mV at pH 8.1, 10 mV at pH 8.8 and 7 mV at pH 9.2 by UV irradiation. The decomposition of CH₃COO⁻ ions and the breakage of the bond between CH₃COO and Zn would be caused by light excitation, ozone and active oxygen by UV irradiation in air. This finding suggests that organic molecules, such as CH₃COO⁻ ions, which show negative zeta potential and can be removed by UV irradiation, would be absorbed onto the surfaces of ZnO crystals. Furthermore, ZnO crystals were confirmed to deposit on a hydrophobic polyethylene terephthalate surface rather than on a hydrophilic polyethylene terephthalate surface modified by UV irradiation in the same solution. Additionally, organic molecule was reported to adsorb to growing ZnO crystals, in which poly (ethylene oxide)-blockpoly (methacrylic acid) (PEO-b-PMAA) was adsorbed preferentially to {0001} face of ZnO to retard crystal growth perpendicular to this face⁶⁰. Consequently, site-selective deposition was achieved by the effective molecular recognition caused by combination of the forces composed mainly of hydrophobic interactions between functional groups of SAMs and ZnO crystal surfaces.

Patterned SAMs were also immersed into the solution containing zinc acetate (15 mM) and ammonia (60 mM or 90 mM) as complexing agent ([NH₃] / [Zn] = 4.0 or 6.0) for 3 h. ZnO crystals having ellipse or multi-needle shape (two large needles and four small needles) were homogeneously nucleated to make the solution turbid shortly after adding ammonia. Nucleation and deposition of ZnO crystals were accelerated by addition of ammonia. Each ZnO crystal was about 500 nm in size. The crystals were deposited and further grown on hydrophobic regions of patterned SAMs selectively. Micropatterns of light-emitting ZnO crystals having ellipse or multi-needle shape were fabricated on patterned SAMs such as OTS-SAM, DTS-SAM, HTS-SAM, PTS-SAM, MTS-SAM, PTCS-SAM or APTS-SAM in aqueous solutions.

XRD spectra of ZnO crystals having ellipse or multi-needle shape showed dominant peaks corresponding to ZnO (0002) planes revealing that ZnO crystals were deposited with a high degree of orientation of their c-axes perpendicular to the substrate. Enhanced (0002) and (10-10) peaks from ZnO crystals having long hexagonal cylinder shape showed that crystals were deposited to make (0002) or (10-10) planes parallel to the substrate. Crystals having high crystallinity and high purity with no additional phase were shown to be prepared in an aqueous solution with precise control of their morphologies without the use of Pd catalyst. The aqueous solution system showed high ability for fabricating nano/micro devices

composed of crystalline materials. ZnO crystals are well known to grow along the c-axis. The orientations evaluated from XRD patterns were consistent with SEM observations and were shown to be controlled precisely by the solution conditions.

Photoluminescence properties of ZnO crystal patterns were further evaluated. Micropatterns of ZnO crystals were observed by an optical microscope (Fig. 9) and strong visible-luminescence from ZnO crystals excited by 330–385 nm light was observed by a photoluminescence microscope. ZnO crystals showed strong UV luminescence (around 390 nm) attributed to band-edge luminescence and visible-light luminescence caused from oxygen vacancy (450–600 nm)^{61,62}. All of the crystals showed photoluminescence due to high purity and high crystallinity with optimal oxygen vacancy, and this caused the bright visible-photoluminescence image. Luminescence properties can be controlled by changing the crystalline morphologies. ZnO crystals deposited from an aqueous solution were shown to have high visible-light-emitting properties.

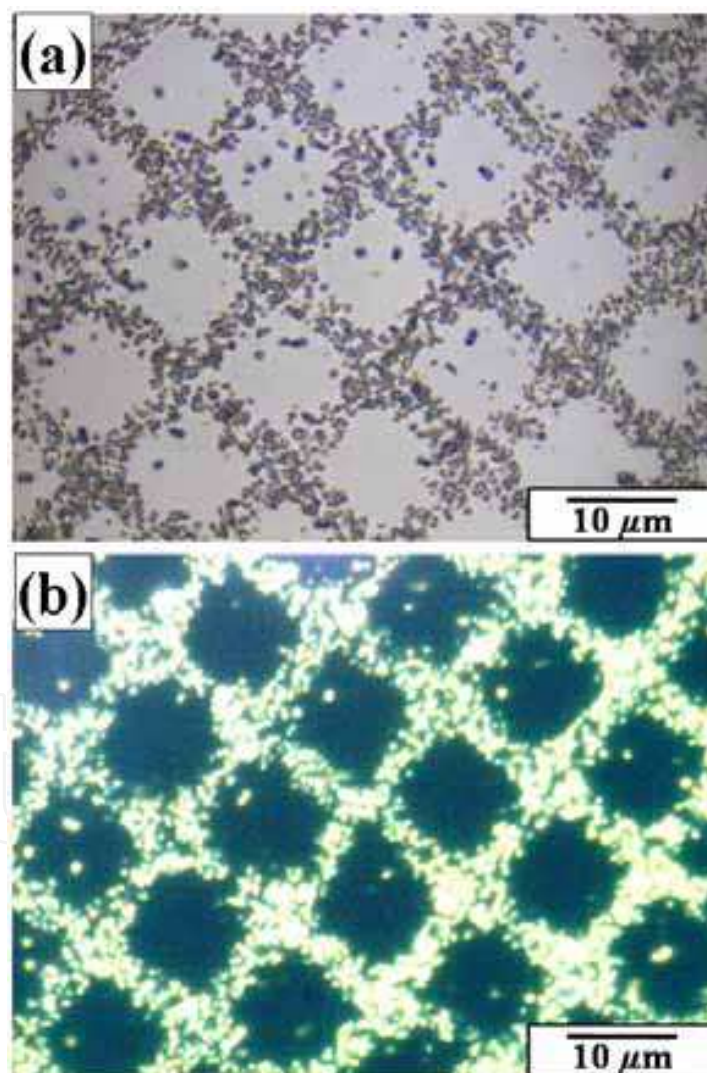


Fig. 9. (a) Optical microscope image and (b) photoluminescence image of patterned ZnO particles under white light or UV light (330–385 nm).

Reprinted with permission from Ref. ³³, Masuda, Y., Kinoshita, N., Sato, F. and Koumoto, K., 2006, *Cryst. Growth Des.*, 6, 75. Copyright © American Chemical Society

2.7 Liquid phase patterning of Y_2O_3 : Eu thin films⁶³

The patterned APTS-SAM was immersed in an aqueous solution containing $Y(NO_3)_3 \cdot 6H_2O$ (4 mM), $Eu(NO_3)_3 \cdot 6H_2O$ (0.4 mM) and NH_2CONH_2 (50 mM) at 25 °C⁶³. The solution was heated to 77 °C gradually as shown in Fig. 10 since urea (NH_2CONH_2) decomposes to form ammonium ions (NH_4^+) above 70 °C (Eq. (a)). The decomposition of urea at elevated temperature plays an essential role in the deposition of yttrium oxide. The aqueous solution of urea yields ammonium ions and cyanate ions (OCN^-) at temperatures above 70 °C⁶⁴ (Eq. (a)). Cyanate ions react rapidly according to Eq. (b). Yttrium ions are weakly hydrolyzed^{65,66} in water to $YOH(H_2O)_n^{2+}$ (Eq. (c)). The resulting release of protons (H^+) and/or hydronium ions (H_3O^+) accelerates urea decomposition (Eq. (b)). The precipitation of the amorphous basic yttrium carbonate ($Y(OH)CO_3 \cdot xH_2O$, $x=1$) can take place through the reaction in Eq. (d)^{67,68}. The controlled release of cyanate ions by urea decomposition causes deposition of basic yttrium carbonate once the critical supersaturation in terms of reacting component is achieved. Since the decomposition of urea is quite slow, the amount needed to reach supersaturation within a given period of time must be considerably higher than the stoichiometric amount of yttrium ions, as revealed by previous studies of lanthanide compounds⁶⁹.

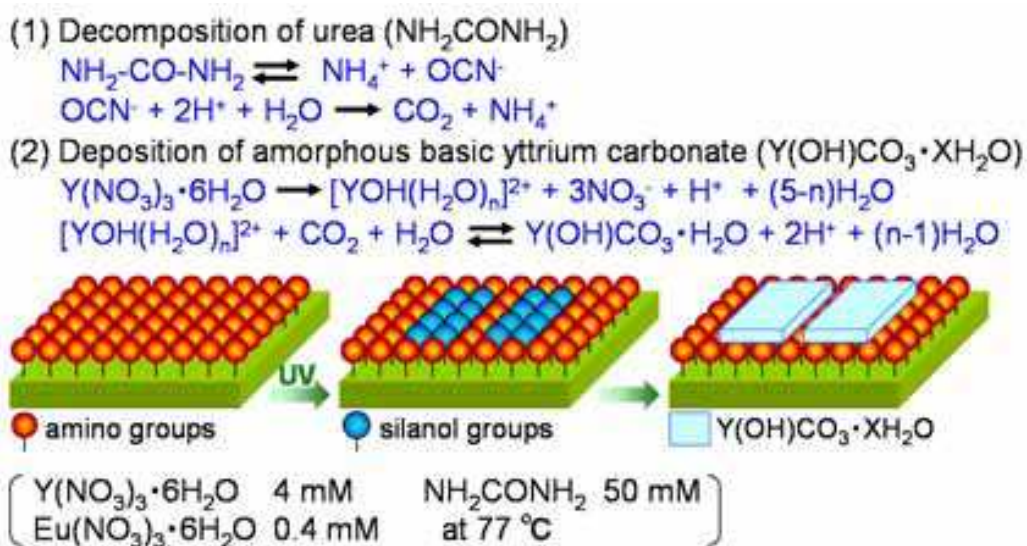


Fig. 10. Conceptual process for site-selective deposition of visible-light emitting Y_2O_3 :Eu thin films using a self-assembled monolayer.

Reprinted with permission from Ref. ⁶³, Masuda, Y., Yamagishi, M. and Koumoto, K., 2007, *Chem. Mater.*, 19, 1002. Copyright © American Chemical Society

The temperature of the solution increased gradually and reached 77 °C in about 80 min. The solution was kept at ~ 77 °C during deposition. The pH of the solution increased from 5.2 to 5.8 in about 90 min and then gradually decreased to 5.6. Temperature and pH increased for the initial 90 min and became stable after 90 min. The average size of particles homogeneously nucleated in the solution at 100 min was about 227 nm and increased to 262 nm at 150 min, 282 nm at 180 min, 310 nm at 210 min, and 323 nm at 240 min. Particles nucleated and grew after the solution temperature exceeded 70 °C because urea decomposes above 70 °C to form carbonate ions⁶⁴ which causes deposition of basic yttrium carbonate⁶⁵⁻⁶⁸. The particles grew rapidly at the beginning of the growth period and then their growth rate

decreased exponentially. The decrease in growth rate was caused by the decrease of supersaturation degree influenced by a decrease in solution concentration.

Yttrium carbonate films were observed to deposit on amino regions of a patterned SAM after the immersion in an aqueous solution (Fig. 11). Deposits showed white contrast, while silanol regions without deposition showed black contrast in SEM observation. Narrow lines of depositions having 10–50 μm width were successfully fabricated in an aqueous solution. Patterned APTS-SAM showed high ability for site-selective deposition of yttrium carbonate in solution systems.

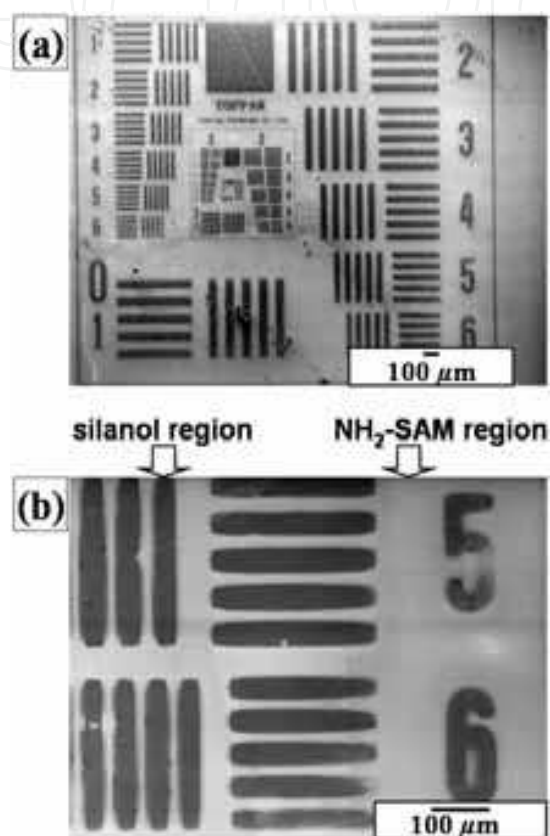


Fig. 11. (a) SEM micrograph of patterned $\text{Y}_2\text{O}_3:\text{Eu}$ thin films and (b) magnified area of (a). Reprinted with permission from Ref. ⁶³, Masuda, Y., Yamagishi, M. and Koumoto, K., 2007, *Chem. Mater.*, 19, 1002. Copyright © American Chemical Society

Yttrium carbonate films were also deposited on the hydrophobic octadecyl surface of OTS(octadecyltrichlorosilane)-SAM having water contact angle (WCA) of 116° and as-purchased silicon wafer having WCA of about $20\text{--}50^\circ$ which was kept in a plastic case in air. On the other hand, the films were not deposited on UV irradiated silicon wafer having $\text{WCA} < 5^\circ$. The super hydrophilic surface of $\text{WCA} < 5^\circ$ suppressed film deposition, whereas the hydrophobic surface and medium surface of $\text{WCA} > 20\text{--}30^\circ$ accelerated film deposition possibly because of hydrophobic interaction between deposition and substrate surface. This is consistent with a former study³². Yttrium carbonate was deposited both on bare single crystal Si wafers, and on Si wafers coated with sulfonate-functionalized organic self-assembled monolayers.

Yttrium, europium, oxygen and carbon were observed from as-deposited thin films on amino regions, while silicon and oxygen were detected from non-covered silanol regions by

EDX. The molecular ratio of yttrium to europium was determined to be 100 : 8. It was close to that of $Y(NO_3)_3 \cdot 6H_2O$ to $Eu(NO_3)_3 \cdot 6H_2O$, i.e., 100 : 10, in the solution because the chemistry of $Eu(NO_3)_3$ is similar to that of $Y(NO_3)_3$ to incorporate europium in the precipitation. The content of europium was in the range we had expected. $Y_2O_3:Eu$ with atomic ratio $Y : Eu = 100 : \sim 8$ was reported to have strong photoluminescence^{70,71}. Carbon was detected from yttrium carbonate. Silicon and oxygen were detected from silicon wafer covered with a natural oxide layer (amorphous SiO_2).

Amino regions were covered with thin films composed of many large particles (about 100–300 nm in diameter) and very high roughness (RMS 25.6 nm). Silanol regions, on the other hand, showed only nano-sized small particles (about 10–50 nm in diameter) and very low roughness (RMS 1.7 nm). The high site-selectivity of deposition and the big difference in surface morphology and roughness were clearly shown by AFM observation. The thickness of the films was estimated from AFM scans across deposited and undeposited regions of the substrate. It increased with immersion time after 45 min (0 nm at 45 min, 60 nm at 70 min and 100 nm at 90 min). The average growth rate (70 nm/h = 100 / 90 min) was higher than that previously reported (2 nm/h = 35 nm / 15 h)⁶⁸. An amorphous yttrium basic carbonate film was deposited at 80 °C from aqueous solutions of $YNO_3 \cdot 5H_2O$ and urea on Si wafers coated with sulfonate-functionalized organic self-assembled monolayers in previous studies. The thickness was then evaluated by TEM after the treatment with ultrasonication for half an hour in distilled water. The difference of growth rate was caused mainly by the difference of the substrate treatment by ultrasonication. Additionally, the thickness of our film was smaller than the particle size in the solution (227 nm at 100 min). Heterogeneous nucleation and attachment of initial particles of yttrium carbonate occurred without the attachment of aggregated large particles. The yttrium carbonate was then grown on the substrate to form a film of 100 nm thickness after immersion for 90 min. The particles of about 100 nm in height were removed by ultrasonication for 30 min and the film of several nm in height remained as reported⁶⁸.

Yttrium was not detected by XPS from the substrate immersed for 45 min, however, it was clearly observed from that immersed for 90 min. This indicates that the deposition began between 45 and 90 min after immersion. The solution temperature reached 70 °C in ~ 45 min and then the solution began to decompose and release carbonate ions, causing the deposition of basic yttrium carbonate. The deposition mechanism evaluated by XPS is consistent with the change of solution temperature, decomposition temperature of urea and chemical reaction of this system. The binding energy of Y 3d_{5/2} spectrum from the deposition (158.2 eV) was higher than that of metal yttrium (155.8 eV)⁷². The spectrum shifted to lower binding energy (156.7 eV) after annealing at 800 °C in air for 1 h and is similar to that of Y_2O_3 (157.0 eV)⁷³. The binding energies of Y 3d_{5/2} spectra in as-deposited films and annealed films were higher than that of metal yttrium possibly due to the chemical bonds formed between yttrium ions and oxygen ions. The chemical shift of Y 3d_{5/2} binding energy by annealing is consistent with crystallization of as-deposited films to crystalline Y_2O_3 . C 1s spectra were detected at 289.7 eV and 284.6 eV from as-deposited films. The C 1s spectrum at 289.7 eV then disappeared by the annealing. C 1s at 284.6 eV was assigned to surface contamination and C 1s at 289.7 eV was detected from as-deposited yttrium carbonate. The disappearance of C 1s at 289.7 eV is consistent with the phase transition from yttrium carbonate to Y_2O_3 .

As-deposited film was shown to be an amorphous phase by XRD measurement. The film showed no diffraction peak after annealing at 400 °C for 1 h, however, it showed 222, 400 and 440 diffraction peaks of crystalline cubic Y_2O_3 ⁷⁴ without any additional phase after annealing at 600 °C for 1 h and the intensities of diffraction peaks increased further by annealing at 800 °C for 1 h. The film was shown to be a polycrystalline Y_2O_3 film constructed from randomly deposited Y_2O_3 particles without crystal-axis orientation. The crystal structure model and diffraction pattern of Y_2O_3 were calculated from the crystal structure data of ICSD #23811. The crystallization by annealing confirmed from XRD measurement is consistent with XPS evaluation.

Y_2O_3 films were attempted to remove from the silicon substrate by debonding with scotch tape or by ultrasonication for 5 min in water. However, the films maintained their bonds with the substrate, indicating that strong adhesion had formed between films and substrate. The thin film annealed at 800 °C for 1 h, i.e., crystalline $Y_2O_3:Eu$ thin film, was shown to be excited by 230–250 nm (center: 243 nm) and emit red light photoluminescence centered at 611 nm in the fluorescence excitation spectrum (Fig. 12a). Neither the as-deposited film nor the film annealed at 400 °C for 1 h showed photoluminescence, on the other hand, the films annealed at 600 °C or 800 °C for 1 h emitted light centered at 617 nm by 250 nm in fluorescence emission spectra (Fig. 12b). The fluorescence intensity of the film annealed at 800 °C was stronger than that of the film annealed at 600 °C. Fluorescence intensity increased by the phase transformation from amorphous yttrium carbonate to yttrium oxide and crystal growth by the heat treatments, and is consistent with the crystallization observed by XRD. The spectra are described by the well-known $^5D_0-^7F_J$ line emissions ($J = 0, 1, 2, \dots$) of the Eu^{3+} ion with the strongest emission for $J = 2$ at 612 nm. The thin film annealed at 800 °C produced visible red light photoluminescence by excitation from Nd:YAG laser (266 nm) (Fig. 12, inset). The white square shows the edges of the $Y_2O_3:Eu$ thin film and the red color shows visible red emission from the irradiated area on the substrate.

2.8 Liquid phase patterning of In_2O_3 thin films⁷⁵

Synthesis and patterning of Pd nanoparticles: A catalyst dispersion^{57,76} containing Na_2PdCl_4 (0.38 mM) and NaCl (0.01 M) in a 0.01 M 2-morpholinoethane sulfonate pH 5 aqueous buffer was prepared (Fig. 13) as described in references^{56,57,76}. Hydrolyzed Pd colloids were formed in this solution⁵⁷. Light-scattering measurements indicated that the catalyst dispersion contained colloid particles of about 30 nm in diameter. Pd nanoparticles showed negative zeta potential (-30.5 eV) at pH 5. APTS-SAM showed positive zeta potential⁷⁷ at pH 5 because of protonation of the amino group ($-NH_2$) to $-NH_3^+$. Silanol groups of UV irradiated APTS-SAM, on the other hand, showed negative zeta potential at pH 5 caused by deprotonation of the silanol group ($-Si-OH$) to $-Si-O^-$. The patterned APTS-SAM was immersed in the colloidal dispersion of catalyst at 25 °C for 30 min and the catalyzed APTS-SAM was rinsed with water. Pd colloids adsorbed on amine groups of APTS-SAM by electrostatic interactions between the negative surface charge of Pd colloids and positive surface charge of APTS-SAM⁵⁴ and formed covalent bonds⁵⁷, while electrostatic repulsion force kept Pd catalyst particles away from silanol group regions having negative zeta potential.

Pd nanoparticles deposited on amino group regions of a patterned SAM had a diameter of about 30 nm and surface roughness (RMS) of about 1 nm as shown by AFM observation

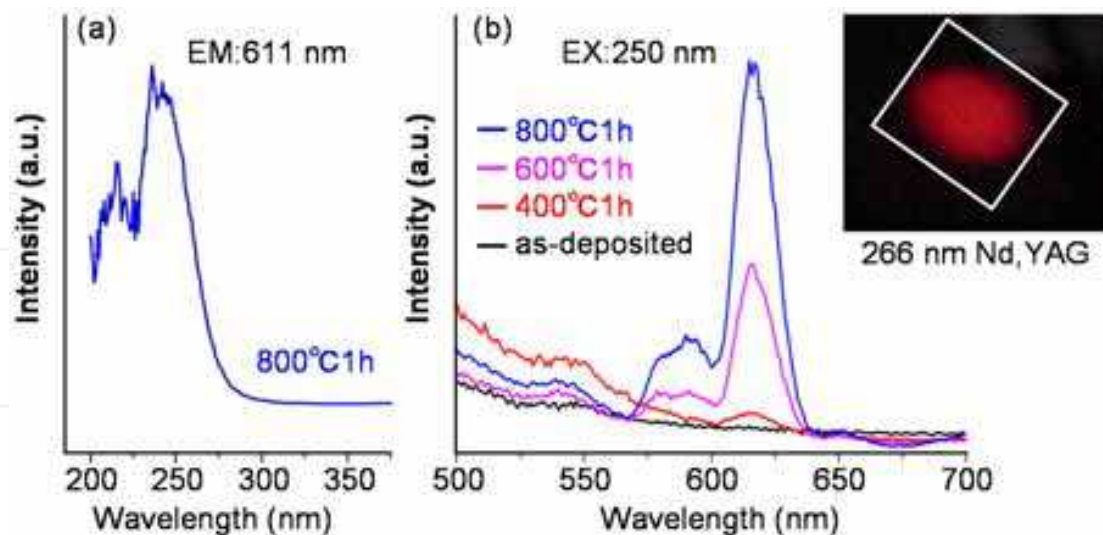


Fig. 12. (a) Fluorescence excitation spectrum (emission: 611 nm) for $\text{Y}_2\text{O}_3:\text{Eu}$ thin film after annealing at 800 °C for 1 h. (b) Fluorescence emission spectra (excitation: 250 nm) for $\text{Y}_2\text{O}_3:\text{Eu}$ thin films before and after annealing at 400, 600 or 800 °C for 1 h. Inset: Photoluminescence image for $\text{Y}_2\text{O}_3:\text{Eu}$ thin film annealed at 800 °C for 1 h (excitation: 266 nm).

Reprinted with permission from Ref. ⁶³, Masuda, Y., Yamagishi, M. and Koumoto, K., 2007, *Chem. Mater.*, 19, 1002. Copyright © American Chemical Society

(Fig. 13). Pd was found to be adsorbed on amino group regions uniformly to form a thin catalytic layer with small surface roughness. Even application, small thickness and small surface roughness of the Pd layer are significant for deposition of a uniform transparent indium oxide layer.

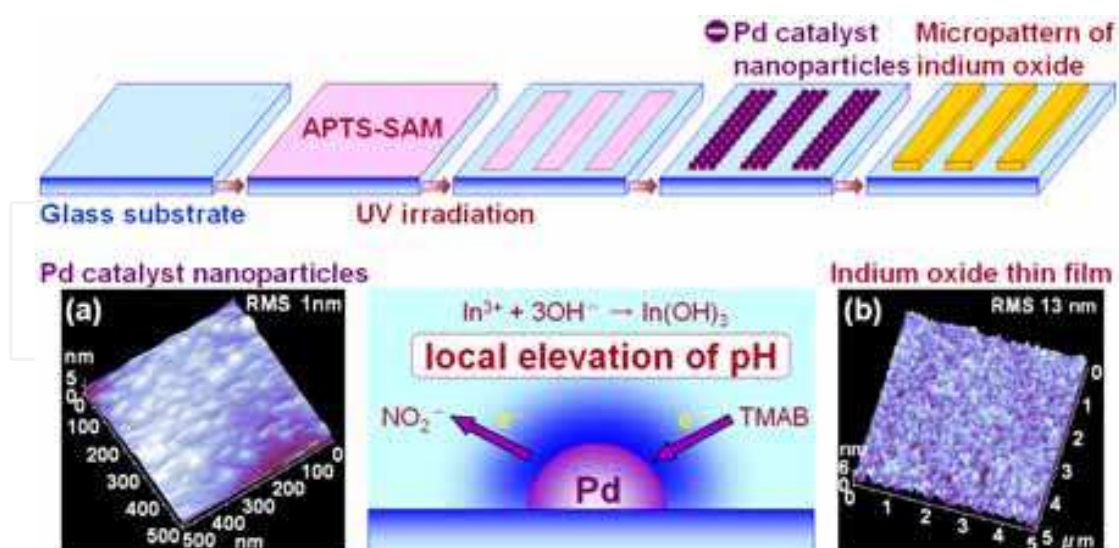


Fig. 13. Conceptual process for micropatterning of indium oxide thin films on a glass substrate. AFM images of (a) Pd catalyst nanoparticles and (b) indium oxide thin films (lower stand).

Reprinted with permission from Ref.⁷⁵, Masuda, Y.; Kondo, M.; Koumoto, K., 2009, *Cryst. Growth Des.*, 9, 555. Copyright © American Chemical Society

Furthermore, site-selective adsorption of Pd was clearly observed by TOF-SIMS mapping⁵⁴. Bright regions due to Pd ($m/z = 104, 105, 106, 108,$ and 110) were observed on the APTS-SAM surface, while no Pd signal was seen on the silanol group surface. This result clearly indicates that site-selective adsorption of Pd catalyst occurred on the APTS-SAM surface.

Deposition control of $\text{In}(\text{OH})_3$ thin films by Pd catalyst: The patterned SAM having Pd catalytic nanoparticles on amino group regions was immersed in an aqueous solution containing $\text{In}(\text{NO}_3)_3$ and TMAB at 65°C for 1 h (Fig. 13).

Nitrate ions were generated by dissolution of indium nitrate in water according to:

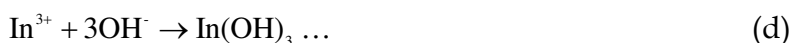


Pd catalyst is indispensable for Eq. (b) and (c). Oxidation of reducing agent, TMAB, is promoted by Pd catalyst to generate electrons in Eq. (b). Nitrate ions are reduced to nitrite ions by receiving electrons according to Eq. (c). Hydroxide ions are generated by oxidation-reduction reactions near Pd catalyst according to Eq. (c). Local elevation of pH thus occurs near Pd catalysts.



$\text{In}(\text{OH})_3$ nucleates and grows at high pH according to Eq. (d).

$\text{In}(\text{OH})_3$ is thus deposited in Pd-adsorbed regions of patterned SAM (Fig. 13).



Transparent conducting In_2O_3 thin film is fabricated by annealing at 300°C in a reduced atmosphere ($3\% - \text{H}_2 / \text{N}_2$) for 1 h according to Eq. (e).



Liquid phase patterning of $\text{In}(\text{OH})_3$ thin films: After having been immersed in the solution containing $\text{In}(\text{NO}_3)_3$ and TMAB, the patterned SAM having Pd catalytic nanoparticles on amino regions was rinsed with distilled water and dried in air. The thin film was clearly shown by SEM observation to deposit on amino group regions selectively (Fig. 14). Silanol group regions and amino group regions of SAM were shown to be black or white, respectively. Magnified SEM micrograph (b) shows the surface morphology of deposited thin films. The thin films were continuous films without micrometer-scale cracks.

The distribution of elements on the surface of the substrates was evaluated by EDX. Indium was detected from thin films on amino group regions selectively and appeared black in EDX mapping images (Fig. 14). On the other hand, silicon was detected mainly from silanol group regions which were not covered with depositions and exposed bare silicon substrate (Fig. 14). These observations showed the site-selective deposition of thin films containing indium on amino group regions.

Surface morphology was further evaluated by AFM conducted at room temperature under ambient air. Thin films were observed on the amino group regions selectively to form micro-scale patterns. The surface of the thin films showed a uniform morphology and low surface roughness $\text{RMS} = 13 \text{ nm}$ (Fig. 13). The thin films deposited on a glass substrate were found

to be transparent, which would be caused by the low surface roughness which reduces diffuse reflection. In-plane particle size was estimated to about 10 – 25 nm in diameter. Film thickness at the edge of the thin film was estimated to be 84 nm.

As-deposited thin film was shown to be crystalline $\text{In}(\text{OH})_3$ (JCPDS No. 16-0161) with no additional phase by XRD evaluation. 002 and 004 diffraction peaks of $\text{In}(\text{OH})_3$ only were detected. $\text{In}(\text{OH})_3$ thin film was shown to have high c-axis orientation. Crystalline size was estimated to be 17.4 nm by using the 002 diffraction peak. This was consistent with the in-plane particle size estimated by AFM observation. Thus, each particle comprising the thin film would be a single crystal.

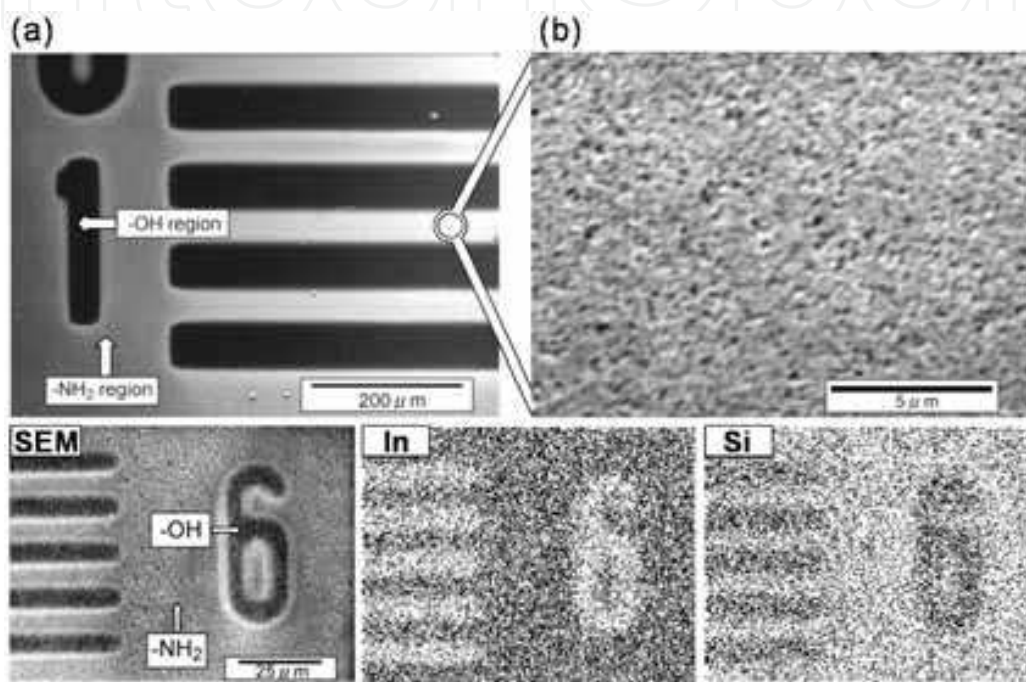


Fig. 14. SEM micrographs of (a) micropattern of indium oxide thin films and (b) magnified area of (a) (upper stand). SEM micrograph and EDX images for In and Si (lower stand). Reprinted with permission from Ref.⁷⁵, Masuda, Y.; Kondo, M.; Koumoto, K., 2009, *Cryst. Growth Des.*, 9, 555. Copyright @ American Chemical Society

Micropatterning of In_2O_3 thin films and its optical properties: $\text{In}(\text{OH})_3$ thin film was annealed at 200, 250 and 300 °C in air. $\text{In}(\text{OH})_3$ thin films transformed into single-phase crystalline In_2O_3 above 250 °C. The film annealed at 300 °C showed 222, 400, 332, 431 and 440 diffraction peaks of In_2O_3 (JCPDS No. 44-1087) with no additional phase. Crystalline size was estimated to be 6.8 nm using the 222 diffraction peak, which was about 0.4 times smaller than that of $\text{In}(\text{OH})_3$.

Thin films maintained their uniform surface morphology in the annealing at 250 °C in air and showed a low surface roughness $\text{RMS} = 11$ nm. In-plane particle size was estimated to be about 10 – 25 nm in diameter. Film thickness on the edge of the thin film was estimated to be 45 nm. Shrinkage of film thickness would be caused by volume decrease during crystallization to In_2O_3 .

The thin films deposited on a glass substrate showed transparency of 60 – 70% in the visible light region and this would be caused by the low surface roughness which reduced diffuse reflection to 5 – 15%.

The optical band gap energy for direct transition in In_2O_3 thin films was estimated to be 3.7 eV assuming that all of the interband transition was direct transition.

Electrical property of In_2O_3 thin films: $\text{In}(\text{OH})_3$ thin film was annealed at 300 °C in a reduced atmosphere (3% - H_2 / N_2) for 1 h instead of atmospheric heating to induce oxygen vacancies to increase the carrier concentration. 222, 400, 332, 431 and 440 diffraction peaks of In_2O_3 (JCPDS No. 44-1087) were observed from the thin film after annealing with no additional phase. Crystalline size was estimated to be 9.8 nm after annealing at 300 °C in a reduced atmosphere using the 222 diffraction peak, which was about 0.6 times smaller than that of $\text{In}(\text{OH})_3$ and slightly larger than that annealed at 300 °C in air.

Carrier concentration and Hall mobility were evaluated to be $2.1 \times 10^{19} \text{ cm}^{-3}$ and $5.2 \text{ cm}^2 \text{ V}^{-1} \text{ s}^{-1}$, respectively by Hall effect measurement. Specific resistance was evaluated to be $5.8 \times 10^{-2} \Omega \text{ cm}$ by the Van der Pauw method. These electrical properties are similar to those of In_2O_3 thin films prepared by the sol-gel method⁷⁸ (carrier concentration: $1.7 \times 10^{19} \text{ cm}^{-3}$, Hall mobility: $5.9 \text{ cm}^2 \text{ V}^{-1} \text{ s}^{-1}$, specific resistance: $6.1 \times 10^{-2} \Omega \text{ cm}$). Electrons would be scattered by grain boundaries in thin films and this would decrease Hall mobility and increase specific resistance. Increase of carrier concentration and decrease of grain boundaries by optimization of the reduction conditions and film formation process would allow us to obtain higher Hall mobility and lower specific resistance, thus improving the electrical properties.

XPS analysis:

(a) XPS analysis for patterning of Pd nanoparticles: Pd was detected from amino group regions of a patterned SAM by XPS. Detection of Pd from amino group regions is consistent with AFM observation and the deposit observed in the AFM image was shown to be Pd colloids particles. On the other hand, Pd was not observed in silanol regions, i.e., UV-irradiated regions of APTS-SAM, even with XPS which is a highly surface sensitive analysis method. Pd adsorption on silanol regions would be less than the detection limit of XPS. High site-selectivity of Pd deposition only on amino group regions of a patterned SAM was shown in XPS analysis.

Pd $3d_{5/2}$ and $3d_{3/2}$ were observed for APTS-SAM at 337.2 eV, 342.5 eV, respectively. The binding energy of Pd $3d_{5/2}$ observed is higher than that of Pd metal (334.6 eV⁷⁹, 335.1 eV⁸⁰⁻⁸²). Referring to an earlier report⁵⁷, the spectrum of Pd $3d_{5/2}$ can be deconvoluted into 3 peaks with peak positions corresponding to Pd-N (338.7 eV)⁸³, Pd-Cl (337.8 eV)⁸⁴⁻⁸⁶ and Pd-O (336.9 eV)⁸⁷ to be Pd-N : Pd-Cl : Pd-O = 0.01 : 0.11 : 0.88⁵⁴ (peak ratio). Pd on the APTS-SAM was mainly combined with O as Pd-O (336.9 eV). This result indicates that the surface of the Pd colloid layer on APTS-SAM consists of Pd-O or Pd-OH as well as a small amount of Pd-Cl. Although the Calvert group reported that the hydrolyzed Pd particles form covalent bonds with other SAMs which have amine groups⁵⁷, the Pd-N bond was not observed in our XPS experiment because of the relatively low depth analyzed by the method (the escape depth of the photoelectrons at the binding energy corresponding to Pd $3d_{5/2}$ is few nanometers), but does not exclude that Pd-N bonds might have been present also in our case.

N 1s spectra of amino group surfaces were detected before and after the immersion into Pd nanoparticle solution, though the spectrum intensities were very low. N1s binding energy of the amino group surface covered with Pd nanoparticles (400.4 eV) was higher than that before immersion (399.6 eV). The positive shift of N1s was about 0.8 eV and is similar to that observed between Pd nanoparticles and the amino group of 3-aminopropyltriethoxysilane-

SAM (about 0.8 eV)⁸⁸. The shift of N 1s would be caused by the decrease of electron cloud density around nitrogen atoms and suggests the formation of chemical bonds between nitrogen atoms and Pd ions. The amino group is a strong electron donor and can coordinate to transition metal ions due to the lone pair electrons of nitrogen atoms. On the other hand, the outermost electron of soft metal ion Pd (II) is constructed from $4d^85s^05p^0$ and has an empty lower energy orbit that can accept electrons. Thus, Pd would form strong bonds with nitrogen rather than oxygen and chloride⁸⁸.

(b) XPS analysis for patterning of $\text{In}(\text{OH})_3$ thin films: XPS spectral peaks corresponding to In $3d_{5/2}$ (445.1 eV), In $3d_{3/2}$ (452.8 eV) and O 1s were observed from $\text{In}(\text{OH})_3$ thin films deposited on the amino group regions.

The binding energy of In $3d_{5/2}$ is higher than that of In metal (443.1⁸⁹, 443.6^{90,91}, 443.8⁹², 444.3 eV⁹³) and In_2O_3 (444.5^{94,95}, 444.6⁹⁶, 444.7^{95,97}, 444.8⁹¹, 444.9⁹⁸ eV), and similar to that of $\text{In}(\text{OH})_3$ (445.0⁸⁰, 445.2 eV⁹⁹). This suggests that the indium atoms in thin films are positively charged relative to that of indium metal by formation of direct bonds with oxygen. The binding energy of In $3d_{5/2}$, which is similar to that of $\text{In}(\text{OH})_3$ rather than In_2O_3 , is consistent with XRD evaluation. On the other hand, this spectrum was not observed from silanol group regions, revealing site-selective deposition of $\text{In}(\text{OH})_3$ thin film.

(c) XPS analysis for patterning of In_2O_3 thin films: The spectral peak corresponding to In $3d_{5/2}$ was shifted to a lower binding energy, 444.9 eV, by annealing at 250 °C in air. This was within the range of that of In_2O_3 and consistent with crystallization into In_2O_3 revealed by XRD evaluation.

Additionally, $\text{In}(\text{OH})_3$ thin film was annealed at 300 °C in a reduced atmosphere (3% - H_2 / N_2) for 1 h instead of atmospheric heating. In $3d_{5/2}$ was shifted to a lower binding energy, 445.0 eV. This was similar to binding energy of $3d_{5/2}$ in In_2O_3 and indicated crystallization of $\text{In}(\text{OH})_3$ into In_2O_3 .

2.9 Liquid phase patterning of crystalline anatase TiO_2 using a superhydrophilic surface¹⁰⁰

A glass substrate coated with an F doped SnO_2 transparent conductive film (FTO, SnO_2 : F, Asahi Glass Co., Ltd., 9.3-9.7 Ω/\square , 26 × 50 × 1.1 mm) showed a water contact angle of 96°. The UV-irradiated surface was, however, wetted completely (contact angle 0-1°). The contact angle decreased with irradiation time (96°, 70°, 54°, 35°, 14°, 5° and 0° for 0 min, 0.5 min, 1 min, 2 min, 3 min, 4 min and 5 min, respectively). This suggests that a small amount of adsorbed molecules on the SnO_2 : F substrate was removed completely by UV irradiation. The surface of the SnO_2 : F substrate would be covered by hydrophilic OH groups after irradiation. Consequently, the SnO_2 : F substrate was modified to have a patterned surface with hydrophobic regions and super-hydrophilic regions.

Aqueous solutions containing ammonium hexafluorotitanate ($[\text{NH}_4]_2\text{TiF}_6$) and boric acid (H_3BO_3) were kept at 50°C for 25h. The substrates were immersed into the solutions at 50°C for 2 h to form a micropattern of TiO_2 .

After having been immersed in the solution, the substrate was rinsed with distilled water and dried in air. The initial FTO surface appeared to be blue-green under white light due to light diffracted from the FTO layer. On the other hand, TiO_2 films deposited on the super-hydrophilic surface appeared to be yellow-green. The color change would be caused by deposition of transparent TiO_2 film which influenced the wavelength of the diffracted light. The micropattern of TiO_2 was shown by SEM evaluation to be successfully fabricated (Fig. 13). TiO_2 deposited on super-hydrophilic regions showed black contrast, while the initial

FTO regions without deposition showed white contrast. The average line width is 55 μm . Line edge roughness³⁴, as measured by the standard deviation of the line width, is $\sim 2.8 \mu\text{m}$. This represents a $\sim 5\%$ variation (i.e., $2.8/55$) in the nominal line width, similar to the usual 5% variation afforded by current electronics design rules. The minimum line width of the pattern depends on the resolution of the photomask and wavelength of irradiated light (184.9 nm). It would be improved to $\sim 1 \mu\text{m}$ by using a high-resolution photomask.

The FTO layer was a particulate film having a rough surface (Fig. 15-b1, b2). Edged particles of 100 – 500 nm in diameter were observed on the surface. The micropattern of TiO_2 thin film was covered by an assembly of nano crystals of 10 – 30 nm in diameter (Fig. 15-a1, a2). The nano crystals would be anatase TiO_2 which grew anisotropically. The TiO_2 film also had large structural relief of 100 – 500 nm in diameter. As the thin TiO_2 film was deposited on the edged particulate surface of the FTO layer, the surface of TiO_2 had large structural relief. The morphology of the TiO_2 layer and FTO layer was further observed by fracture cross section profiles (Fig. 16). The polycrystalline FTO layer prepared on a flat glass substrate was shown to have a thickness of $\sim 900 \text{ nm}$, and a high roughness of 100 – 200 nm on the surface (Fig. 16a). Nano TiO_2 crystals were deposited on the super-hydrophilic FTO surface (Fig. 16a), whereas no deposition was observed on the initial FTO surface. The super-hydrophilic FTO surface was covered with an array of nano TiO_2 crystals (Fig. 16b, c), which had a long shape of $\sim 150 \text{ nm}$ in length and $\sim 20 \text{ nm}$ in diameter. These observations were consistent with TEM and XRD evaluations⁹⁹. Nano TiO_2 crystals would grow along the c-axis and thus enhance the 004 X-ray diffraction peak and 004 electron diffraction peak. They formed a long shape having a high aspect ratio of 7.5 (150 nm in length / 20 nm in diameter) as shown in the SEM fracture cross section profile (Fig. 16b, c) and TEM micrograph⁹⁹. The orientation of nano TiO_2 crystals with their long axis perpendicular to the FTO layer (Fig. 16b, c) would also enhance the 004 diffraction peak.

The film deposited on the substrate was evaluated by XRD analysis. Strong X-ray diffractions were observed for films deposited on FTO substrates and assigned to SnO_2 of FTO films. The 004 diffraction peak of anatase TiO_2 was not observed clearly for TiO_2 film on FTO substrates because both of the weak 004 diffraction peak of TiO_2 and the strong diffraction peak of FTO were observed at the same angle. Glass substrates with no FTO coating were immersed in the solution. Weak X-ray diffraction peaks were observed at $2\theta = 25.3, 37.7, 48.0, 53.9, 55.1$ and 62.7° for the films deposited on glass substrates. They were assigned to 101, 004, 200, 105, 211 and 204 diffraction peaks of anatase TiO_2 (ICSD No. 9852). A broad diffraction peak from the glass substrate was also observed at about $2\theta = 25^\circ$.

The intensity of the 004 diffraction peak was stronger than that of the 101 diffraction peak for the film obtained by the liquid phase crystal deposition method, though the intensity of 101 was stronger than that of 004 for anatase TiO_2 powders with no orientation (ICSD No. 9852). The integral intensity or peak height of 004 was 2.6 times or 2.2 times that of 101, respectively, suggesting high c-axis orientation of anatase TiO_2 crystals. Crystallite size perpendicular to the 101 or 004 planes was estimated from the full-width half-maximum of the 101 or 004 peak to be 9 nm or 17 nm, respectively. Elongation of crystals in the c-axis direction was also suggested by the difference of crystallite size. These evaluations were consistent with high c-axis orientation observed by TEM and electron diffraction⁹⁹. Crystallite size estimated by XRD was similar to that in TiO_2 under layer rather than that of acicular crystals observed by TEM. TiO_2 thin film prepared on a glass would be constructed of not acicular crystals but polycrystals in under layer.

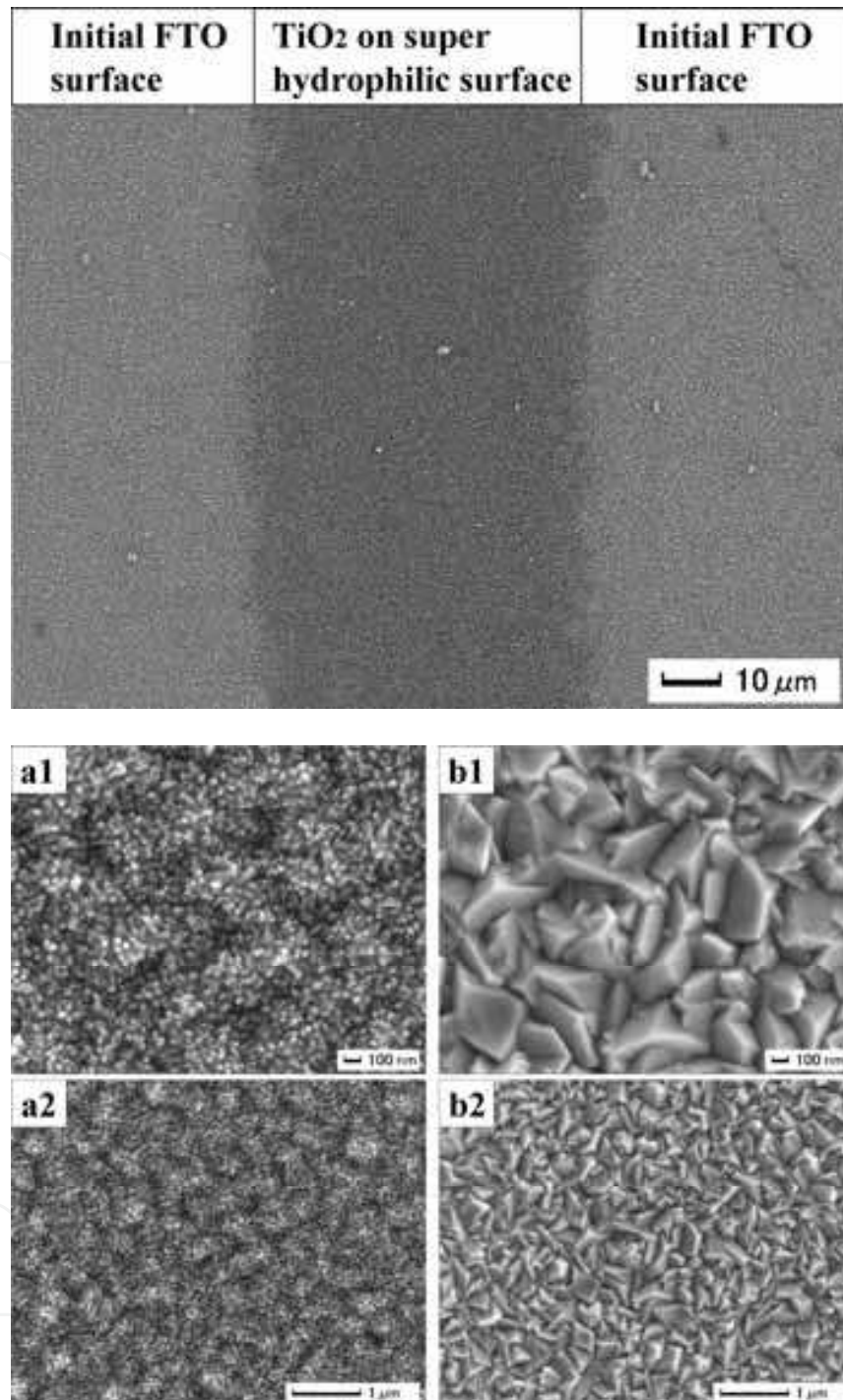


Fig. 15. SEM micrograph of a micropattern of anatase TiO₂ films on SnO₂: F substrates. (a1) Surface of anatase TiO₂ films deposited on super-hydrophilic region. TiO₂ was formed on super-hydrophilic region which was cleaned by UV irradiation before the immersion. (a2) Magnified area of (a1) showing surface morphology of anatase TiO₂ film. (b1) Surface of SnO₂: F substrate without TiO₂ deposition. TiO₂ was not formed on non-cleaned region. (b2) Magnified area of (b1) showing surface morphology of SnO₂: F substrate. Reprinted with permission from Ref.¹⁰⁰, Masuda, Y. and Kato, K., 2008, *Chem. Mater.*, 20, 1057. Copyright © American Chemical Society

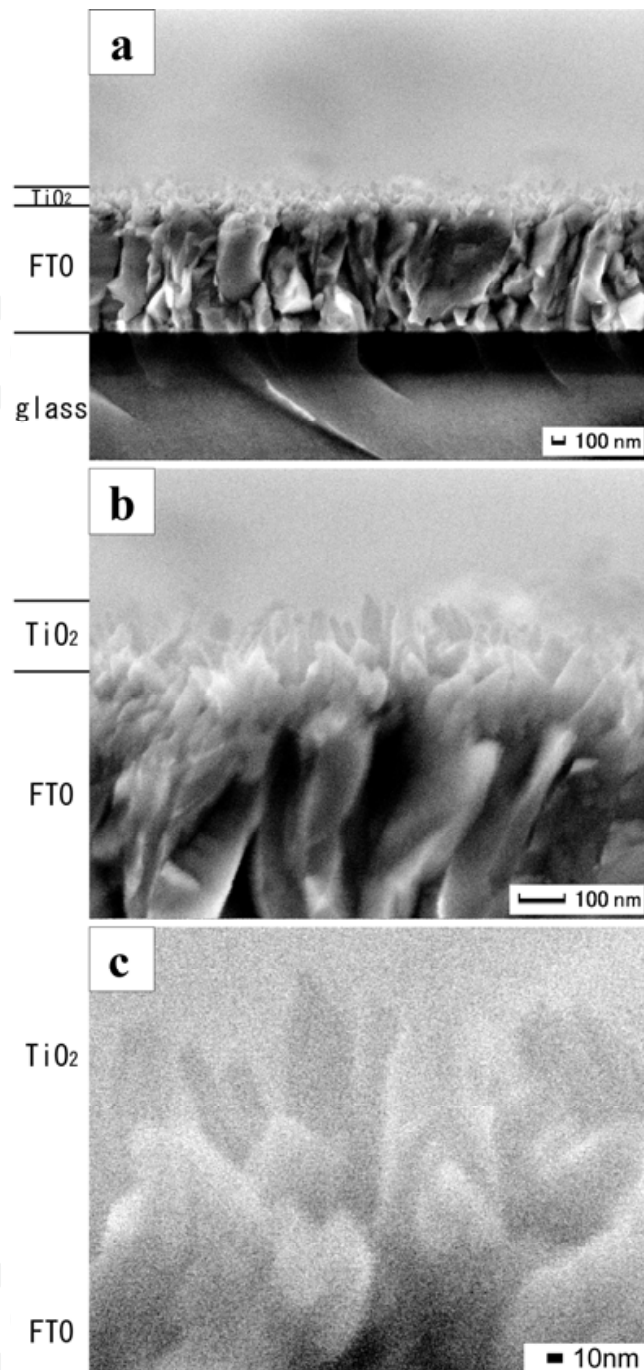


Fig. 16. SEM micrographs of anatase TiO₂ films on SnO₂: F substrates. (a) Fracture cross section of TiO₂ films. (b, c) Magnified area of (a) showing morphology of nano TiO₂ crystals. Reprinted with permission from Ref.¹⁰⁰, Masuda, Y. and Kato, K., 2008, *Chem. Mater.*, 20, 1057. Copyright © American Chemical Society

3. Summary

A novel concept “Liquid Phase Patterning” was proposed based on scientific knowledge obtained from investigations of interactions and chemical reactions between functional groups of SAMs and ions, clusters and homogeneously nucleated particles in solutions. Nano/micropatterns of metal oxides such as TiO₂, Fe₃O₄, ZnO, etc. were successfully

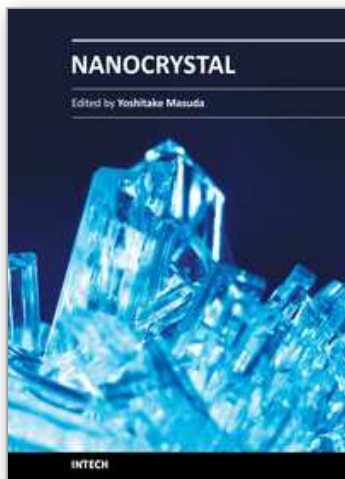
fabricated on a patterned SAM. Mechanisms were further discussed. These studies showed high performance and high potential of solution chemistry for inorganic materials. The novel concepts and technologies in these studies would open new doors for next generation ceramic science.

4. References

- [1] http://www.epa.gov/greenchemistry/whats_gc.html.
- [2] Anastas, P. T.; Warner, J. C. *Green Chemistry: Theory and Practice*; Oxford University Press: New York, 1998.
- [3] <http://www.meti.go.jp/policy/chemistry/>.
- [4] *Green chemistry workshop, Ministry of Economy, Trade and Industry Japan*, 1999.
- [5] <http://www.rsc.org/is/journals/current/green/greenpub.htm>.
- [6] <http://www.gdch.de/>.
- [7] Mann, S. *Biomimetic Materials Chemistry*; VCH Publishers: Weinheim, 1996.
- [8] Yoshimura, M.; Livage, J. *MRS Bulletin* 2000, 25, 12-13.
- [9] Yoshimura, M.; Suchanek, W. L.; Byrappa, K. *MRS Bull.* 2000, 25, 17-25.
- [10] Yoshimura, M. *J. Mater. Res.* 1998, 13, 796-802.
- [11] Figlarz, M. *Chem. Scr.*, 1988, 28, 3-7.
- [12] Niesen, T. P.; DeGuire, M. R. *J. Electroceram.* 2001, 6, 169-207.
- [13] Pizem, H.; Sukenik, C. N.; Sampathkumaran, U.; McIlwain, A. K.; De Guire, M. R. *Chem. Mater.* 2002, 14, 2476-2485.
- [14] Lev, O.; Wu, Z.; Bharathi, S.; Glezer, V.; Modestov, A.; Gun, J.; Rabinovich, L.; Sampath, S. *Chem. Mater.* 1997, 9, 2354-2375.
- [15] Klein, L. *Sol-Gel Optics: Processing and Applications*; Kluwer Academic Publishers: Boston, 1994.
- [16] Byrappa, K.; Yoshimura, M. *Handbook of Hydrothermal Technology*; LLC/Noyes Publications: Park Ridge, NJ, 2000.
- [17] Yoshimura, M.; Suchanek, W. *Solid State Ionics* 1997, 98, 197-208.
- [18] Yoshimura, M.; Suchanek, W.; Han, K. S. *J. Mater. Chem.* 1999, 9, 77-82.
- [19] Cho, Y. R.; Lee, J. H.; Song, Y. H.; Kang, S. Y.; Hwang, C. S.; Jung, M. Y.; Kim, D. H.; Lee, S. K.; Uhm, H. S.; Cho, K. I. *Mater. Sci. Eng. B* 2001, 79, 128-132.
- [20] Jeon, N. L.; Clem, P. G.; Nuzzo, R. G.; Payne, D. A. *Journal of Materials Research* 1995, 10, 2996-2999.
- [21] Aizenberg, J.; Braun, P. V.; Wiltzius, P. *Phys. Rev. Lett.* 2000, 84, 2997-3000.
- [22] Nashimoto, K.; Haga, K.; Watanabe, M.; Nakamura, S.; Osakabe, E. *Appl. Phys. Lett.* 1999, 75, 1054-1056.
- [23] Mott, M.; Song, J. H.; Evans, J. R. G. *J. Am. Ceram. Soc.* 1999, 82, 1653-1658.
- [24] Stutzmann, N.; Tervoort, T. A.; Bastiaansen, C. W. M.; Feldman, K.; Smith, P. *Adv. Mater.* 2000, 12, 557-562.
- [25] Matsuda, A.; Matsuno, Y.; Tatsumisago, M.; Minami, T. *J. Am. Ceram. Soc.* 1998, 81, 2849-2852.
- [26] Bauer, W.; Ritzhaupt-Kleissl, H. J.; Hausselt, J. *Ceram. Inter.* 1999, 25, 201-205.
- [27] Jacobs, H. O.; Whitesides, G. M. *Science* 2001, 291, 1763-1766.
- [28] Kim, E.; Xia, Y. N.; Whitesides, G. M. *Nature* 1995, 376, 581-584.
- [29] Kim, C.; Burrows, P. E.; Forrest, S. R. *Science* 2000, 288, 831-833.
- [30] Masuda, Y. <http://staff.aist.go.jp/masuda-y/index.html>.

- [31] Masuda, Y.; Gao, Y. F.; Zhu, P. X.; Shirahata, N.; Saito, N.; Koumoto, K. *J. Ceram. Soc. Japan* 2004, 112, 1495-1505.
- [32] Masuda, Y. *J. Jpn. Soc. Powder Metallurgy* 2007, 54, 854-862.
- [33] Masuda, Y.; Kinoshita, N.; Sato, F.; Koumoto, K. *Cryst. Growth Des.* 2006, 6, 75-78.
- [34] Masuda, Y.; Sugiyama, T.; Lin, H.; Seo, W. S.; Koumoto, K. *Thin Solid Films* 2001, 382, 153-157.
- [35] Masuda, Y.; Jinbo, Y.; Yonezawa, T.; Koumoto, K. *Chem. Mater.* 2002, 14, 1236-1241.
- [36] Masuda, Y.; Wang, D. J.; Yonezawa, T.; Koumoto, K. *Key Eng. Mater.* 2002, 228-229, 125-130.
- [37] Wang, D. J.; Masuda, Y.; Seo, W. S.; Koumoto, K. *Key Eng. Mater.* 2002, 214, 163-168.
- [38] Lee, L. H. *Journal of Colloid and Interface Science* 1968, 27, 751-760.
- [39] Masuda, Y.; Ieda, S.; Koumoto, K. *Langmuir* 2003, 19, 4415-4419.
- [40] Masuda, Y.; Saito, N.; Hoffmann, R.; De Guire, M. R.; Koumoto, K. *Sci. Tech. Adv. Mater.* 2003, 4, 461-467.
- [41] Masuda, Y.; Sugiyama, T.; Koumoto, K. *J. Mater. Chem.* 2002, 12, 2643-2647.
- [42] Gun, J.; Sagiv, J. *J. Colloid Interface Science* 1986, 112, 457-472.
- [43] McGovern, M. E.; Kallury, K. M. R.; Thompson, M. *Langmuir* 1994, 10, 3607-3614.
- [44] Duchet, J.; Chabert, B.; Chapel, J. P.; Gerard, J. F.; Chovelon, J. M.; Jaffrezic-Renault, N. *Langmuir* 1997, 13, 2271-2278.
- [45] Dressick, W. J.; Chen, M.-S.; Brandow, S. L. *J. Amer. Chem. Soc.* 2000, 122, 982-983.
- [46] Dressick, W. J.; Chen, M.-S.; Brandow, S. L.; Rhee, K. W.; Shirey, L. M.; Perkins, F. K. *Appl. Phys. Lett.* 2001, 78, 676-678.
- [47] Dressick, W. J.; Nealey, P. F.; Brandow, S. L. *Proc. SPIE* 2001, 4343, 294-305.
- [48] Koumoto, K.; Seo, S.; Sugiyama, T.; Seo, W. S.; Dressick, W. J. *Chem. Mater.* 1999, 11, 2305.
- [49] Masuda, Y.; Sugiyama, T.; Seo, W. S.; Koumoto, K. *Chem. Mater.* 2003, 15, 2469-2476.
- [50] Collins, R. J.; Shin, H.; De Guire, M. R.; Heuer, A. H.; Sukenik, C. N. *Appl. Phys. Lett.* 1996, 69, 860-862.
- [51] Huang, D.; Xiao, Z. D.; Gu, J. H.; Huang, N. P.; Tuan, C.-W. *Thin Solid Films* 1997, 305, 110-115.
- [52] Zhang, F.; Mao, Y.; Zheng, Z.; Chen, Y.; Liu, X.; Jin, S. *Thin Solid Films* 1997, 310, 29-33.
- [53] Shin, H.; Collins, R. J.; DeGuire, M. R.; Heuer, A. H.; Sukenik, C. N. *J. Mater. Res.* 1995, 10, 699-703.
- [54] Nakanishi, T.; Masuda, Y.; Koumoto, K. *Chem. Mater.* 2004, 16, 3484-3488.
- [55] Nakanishi, T.; Masuda, Y.; Koumoto, K. *J. Cryst. Growth* 2005, 284, 176-183.
- [56] Brandow, S. L.; Dressick, W. J.; Marrian, C. R. K.; Chow, G. M.; Calvert, J. M. *J. Electrochem. Soc.* 1995, 142, 2233-2243.
- [57] Dressick, W. J.; Dulcey, C. S.; Georger, J. H.; Calabrese, G. S.; Calvert, J. M. *J. Electrochem. Soc.* 1994, 141, 210-220.
- [58] Izaki, M.; Shinoura, O. *Adv. Mater.* 2001, 13, 142-145.
- [59] Call, R. L.; Jaber, N. K.; Seshan, K.; Whyte, J. R. *Solar Energy Mater.* 1980, 2, 373-380.
- [60] Oner, M.; Norwig, J.; Meyer, W. H.; Wegner, G. *Chem. Mater.* 1998, 10, 460-463.
- [61] Wu, X. L.; Siu, G. G.; Fu, C. L.; Ong, H. C. *Appl. Phys. Lett.* 2001, 78, 2285-2287.
- [62] Kang, J. S.; Kang, H. S.; Pang, S. S.; Shim, E. S.; Lee, S. Y. *Thin Solid Films* 2003, 443, 5-8.
- [63] Masuda, Y.; Yamagishi, M.; Koumoto, K. *Chem. Mater.* 2007, 19, 1002-1008.
- [64] Shaw, W. H. R.; Bordeaux, J. J. *J. Am. Chem. Soc.* 1955, 77, 4729-4733.
- [65] Ryabchikov, D. E.; Ryabukhin, V. A. *Analytical Chemistry of Yttrium and the Lanthanide Elements*; Humphrey Science: Ann Arbor, MI, 1970.

- [66] Baes, C. F.; Mesmer, R. E. *The Hydrolysis of Captions*; Wiley: New York, 1976.
- [67] Aiken, B.; Hsu, W. P.; Matijevic, E. J. *Am. Ceram. Soc.* 1988, 71, 845-853.
- [68] Agarwal, M.; DeGuire, M. R.; Heuer, A. H. *Appl. Phys Lett.* 1997, 71, 891-893.
- [69] Matijevic, E.; Hsu, W. P. *J. Colloid Interface Sci.* 1987, 118, 506-523.
- [70] Sharma, P. K.; Jilavi, M. H.; Nass, R.; Schmidt, H. J. *Lumin.* 1999, 82, 187-193.
- [71] Kwaka, M. G.; Parkb, J. H.; Shon, S. H. *Solid State Commun.* 2004, 130, 199-201.
- [72] Fuggle, J. C.; Martensson, N. J. *Electron Spectrosc. Relat. Phenom.* 1980, 21, 275.
- [73] Wagner, C. D. *Practical Surface Analysis*; 2 ed.; John Wiley, 1990; Vol. 1.
- [74] Paton, M. G.; Maslen, E. N. *Acta Crystallographica* 1967, 1, 1948-23.
- [75] Masuda, Y.; Kondo, M.; Koumoto, K. *Crystal Growth & Design* 2009, 9, 555-561.
- [76] Dressick, W. J.; Kondracki, L. M.; Chen, M. S.; Brandow, S. L.; Matijevic, E.; Calvert, J. M. *Colloids and Surfaces A-Physicochemical and Engineering Aspects* 1996, 108, 101-111.
- [77] Masuda, Y.; Koumura, T.; Okawa, T.; Koumoto, K. *J. Colloid Interface Sci.* 2003, 263, 190-195.
- [78] Tahar, R. B. H.; Ban, T.; Ohya, Y.; Takahashi, Y. *J. Appl. Phys.* 1997, 82, 865-870.
- [79] Hilaire, L.; Legare, P.; Holl, Y.; Maire, G. *Solid State Commun.* 1979, 32, 157-160.
- [80] Wagner, C. D.; Riggs, W. M.; Davis, L. E.; Moulder, J. F.; Muilenberg, G. E. *Handbook of X-ray Photoelectron Spectroscopy*; Perkin-Elmer Corp., Physical Electronics Div., Eden Prairie: Minnesota, 1979.
- [81] Weightman, P.; Andrews, P. T. *J. Phys. C-Solid State Phys.* 1980, 13, L815-L819.
- [82] Weightman, P.; Andrews, P. T. *J. Phys. C-Solid State Phys.* 1980, 13, L821-L825.
- [83] Nefedov, V. I.; Zakharova, I. A.; Moiseev, I. I.; Porai-koshits, M. A.; Vargoftik, M. N.; Belov, A. P. *Zh. Neorg. Khim.* 1973, 18, 3264-3268.
- [84] Nefedov, V. I.; Kokunov, Y. V.; Buslaev, Y. A.; Poraikos.Ma; Gustyako.Mp; Ilin, E. G. *Zhurnal Neorganicheskoi Khimii* 1973, 18, 931-934.
- [85] Choudary, B. M.; Kumar, K. R.; Jamil, Z.; Thyagarajan, G. *Journal of the Chemical Society-Chemical Communications* 1985, 931-932.
- [86] Sakurada, O.; Takahashi, H.; Taga, M. *Bunseki Kagaku* 1989, 38, 407-412.
- [87] Datye, A. K.; Bravo, J.; Nelson, T. R.; Atanasova, P.; Lyubovsky, M.; Pfefferle, L. *Applied Catalysis a-General* 2000, 198, 179-196.
- [88] Bazzicalupi, C.; Bencini, A.; Bianchi, A.; Giorgi, C.; Valtancoli, B. *Coordination Chemistry Reviews* 1999, 184, 243-270.
- [89] Ouchene M., S. C., Belin E., Gheorghiu A., Theye M. *J. Non-Cryst. Solids* 1983, 59&60, 625-628.
- [90] Bertrand, P. A. *J. Vac. Sci. Technol.* 1981, 18, 28-33.
- [91] Kazmerski, L. L.; Jamjoum, O.; Ireland, P. J.; Deb, S. K.; Mickelsen, R. A.; Chen, W. J. *Vac. Sci. Technol.* 1981, 19, 467-471.
- [92] Sen, P.; Hegde, M. S.; Rao, C. N. *Appl. Surf. Sci.* 1982, 10, 63.
- [93] Wagner, C. D. *Discuss. Faraday Soc.* 1975, 60,, 291.
- [94] Fan, J. C. C.; Goodenough, J. B. *J. Appl. Phys.* 1977, 48, 3524-3531.
- [95] Lin, A. W. C.; Armstrong, N. R.; Kuwana, T. *Anal. Chem.* 1977, 49, 1228-1235.
- [96] Clark, D. T.; Fok, T.; Roberts, G. G.; Sykes, R. W. *Thin Solid Films* 1980, 70, 261-283.
- [97] Cahen, D.; Ireland, P. J.; Kazmerski, L. L.; Thiel, F. A. *J. Appl. Phys.* 1985, 57, 4761-4771.
- [98] Hewitt, R. W.; Winograd, N. *J. Appl. Phys.* 1980, 51, 2620-2624.
- [99] Faur, M.; Faur, M.; Jayne, D. T.; Goradia, M.; Goradia, C. *Surf. Interface Anal.* 1990, 15, 641-650.
- [100] Masuda, Y.; Kato, K. *Chem. Mater.* 2008, 20, 1057-1063.



Nanocrystal

Edited by Dr. Yoshitake Masuda

ISBN 978-953-307-199-2

Hard cover, 494 pages

Publisher InTech

Published online 28, June, 2011

Published in print edition June, 2011

We focused on cutting-edge science and technology of Nanocrystals in this book. “Nanocrystal” is expected to lead to the creation of new materials with revolutionary properties and functions. It will open up fresh possibilities for the solution to the environmental problems and energy problems. We wish that this book contributes to bequeath a beautiful environment and valuable resources to subsequent generations.

How to reference

In order to correctly reference this scholarly work, feel free to copy and paste the following:

Yoshitake Masuda (2011). Nano/Micro-Patterning of Metal Oxide Nanocrystals, Nanocrystal, Dr. Yoshitake Masuda (Ed.), ISBN: 978-953-307-199-2, InTech, Available from:

<http://www.intechopen.com/books/nanocrystal/nano-micro-patterning-of-metal-oxide-nanocrystals>

INTECH
open science | open minds

InTech Europe

University Campus STeP Ri
Slavka Krautzeka 83/A
51000 Rijeka, Croatia
Phone: +385 (51) 770 447
Fax: +385 (51) 686 166
www.intechopen.com

InTech China

Unit 405, Office Block, Hotel Equatorial Shanghai
No.65, Yan An Road (West), Shanghai, 200040, China
中国上海市延安西路65号上海国际贵都大饭店办公楼405单元
Phone: +86-21-62489820
Fax: +86-21-62489821

© 2011 The Author(s). Licensee IntechOpen. This chapter is distributed under the terms of the [Creative Commons Attribution-NonCommercial-ShareAlike-3.0 License](#), which permits use, distribution and reproduction for non-commercial purposes, provided the original is properly cited and derivative works building on this content are distributed under the same license.

IntechOpen

IntechOpen